

Time-resolved rotational velocities in the upper atmosphere of WASP-33 b*

P. WILSON CAULEY,¹ JI WANG,² EVGENYA L. SHKOLNIK,³ ILYA ILYIN,⁴ KLAUS G. STRASSMEIER,⁴ SETH REDFIELD,⁵ AND ADAM JENSEN⁶

¹*Laboratory for Atmospheric and Space Physics, University of Colorado Boulder, Boulder, CO 80303*

²*Department of Astronomy, Ohio State University, Columbus, OH 43210*

³*Arizona State University, School of Earth and Space Exploration, Tempe, AZ 85287*

⁴*Leibniz-Institute for Astrophysics Potsdam (AIP), An der Sternwarte 16, 14482, Potsdam, Germany*

⁵*Wesleyan University, Astronomy Department, Van Vleck Observatory, Middletown, CT 06459*

⁶*Department of Physics and Astronomy, University of Nebraska at Kearney, Kearney, NE 68849*

(Received 08/26/2020; Accepted)

Submitted to AAS journals

ABSTRACT

While steady empirical progress has been made in understanding the structure and composition of hot planet atmospheres, direct measurements of velocity signatures, including winds, rotation, and jets, have lagged behind. Quantifying atmospheric dynamics of hot planets is critical to a complete understanding of their atmospheres and such measurements may even illuminate other planetary properties, such as magnetic field strengths. In this manuscript we present the first detection of the Balmer lines H α and H β in the atmosphere of the ultra-hot Jupiter WASP-33 b. Using atmospheric models which include the effects of atmospheric dynamics, we show that the shape of the average Balmer line transmission spectrum is consistent with rotational velocities in the planet's thermosphere of $v_{\text{rot}} = 10.1^{+0.8}_{-1.0}$ km s⁻¹. We also measure a low-significance blue-shift of $-4.6^{+3.4}_{-3.4}$ km s⁻¹ in the transmission spectrum which is naturally explained by a global wind across the planet's terminator. In a separate analysis the time-resolved velocity centroids of individual transmission spectra show unambiguous evidence of rotation, with a best-fit velocity of $8.5^{+2.1}_{-1.9}$ km s⁻¹, consistent with the value of v_{rot} derived from the shape of the average Balmer line transmission spectrum. Our observations demonstrate the power of high signal-to-noise, time-resolved transmission spectra to measure the effects of velocity structures in exoplanet atmospheres. The large rotational and wind velocities we measure highlight the need for more detailed 3D global climate simulations of the rarefied upper-atmospheres of ultra-hot gas giants.

1. INTRODUCTION

The characterization of hot exoplanet atmospheres has advanced steadily over the past decade, with details continuously being revealed about the diversity of thermal profiles (Line et al. 2016; Evans et al. 2017; Nugroho

et al. 2017; Nikolov et al. 2018; Gibson et al. 2020; Yan et al. 2020; Baxter et al. 2020), chemical abundances (Line et al. 2014; Brogi & Line 2019; Pino et al. 2020), atmospheric evaporation processes (Bourrier et al. 2013; Ehrenreich et al. 2015; Lavie et al. 2017; Bourrier et al. 2018), and the presence of clouds and hazes (Kreidberg et al. 2014; Barstow et al. 2017; Moran et al. 2018; Beatty et al. 2019; Libby-Roberts et al. 2020; Gao et al. 2020). Recent observations of hot planet atmospheres at high spectral resolution, both in transmission and via cross-correlation of thermal emission signatures, have accelerated the detection of a wide variety of molecular and atomic species (e.g., Casasayas-Barris et al. 2017; Jensen et al. 2018; Spake et al. 2018; Allart et al. 2018; Salz et al. 2018; Hoeijmakers et al. 2018, 2019; Cauley et al. 2019a; Sing et al. 2019; Brogi & Line 2019; Yan et al. 2019; Keles et al. 2019; von Essen et al. 2019;

Corresponding author: P. Wilson Cauley
pwcauley@gmail.com

* Based on data acquired with PEPSI using the Large Binocular Telescope (LBT). The LBT is an international collaboration among institutions in the United States, Italy, and Germany. LBT Corporation partners are the University of Arizona on behalf of the Arizona university system; Istituto Nazionale di Astrofisica, Italy; LBT Beteiligungsgesellschaft, Germany, representing the Max-Planck Society, the Leibniz-Institute for Astrophysics Potsdam (AIP), and Heidelberg University; the Ohio State University; and the Research Corporation, on behalf of the University of Notre Dame, University of Minnesota and University of Virginia.

Turner et al. 2020; Nugroho et al. 2020a,b; Ben-Yami et al. 2020; Stangret et al. 2020).

The direct observation of velocity signatures has, however, lagged behind the otherwise remarkable progress made in understanding the properties of hot planet atmospheres. Quantifying velocity dynamics such as rotation, equatorial jets, and hydrodynamic expansion can reveal crucial information about related planetary properties, such as magnetic fields (Cauley et al. 2019b), heat redistribution efficiency and mass loss rates (Showman & Guillot 2002; Miller-Ricci Kempton & Rauscher 2012; Spiegel & Burrows 2013), and provide important feedback to global climate simulations (GCMs) (Showman & Polvani 2011; Rauscher & Menou 2013; Carone et al. 2020). Thermal phase curves and low-resolution spectra, while not directly measuring the Doppler shifts of atmospheric gas, have been used to infer the presence of heat redistribution by winds and jets (e.g., Knutson et al. 2012; Kataria et al. 2015; Wong et al. 2016; Rogers 2017; Wong et al. 2020; von Essen et al. 2020). Wind speeds have also been inferred for brown dwarfs using IR and radio variability (Apai et al. 2017; Allers et al. 2020). In addition to the relative dearth of observed velocity signatures, there is also a critical lack of GCMs which take into account the most rarefied bound atmospheric layers at pressures $p < 10^{-3}$ bar, i.e. the thermosphere, that are typically sampled with transmission spectroscopy of atomic ions.

The first measurement of rotational broadening in an exoplanet atmosphere was performed by Snellen et al. (2014) who constrained the equatorial rotation velocity of the young planet β Pic b to $v_{\text{rot}} = 25.0 \pm 3.0$ km s $^{-1}$ using emission features of CO and H $_2$ O. Such large rotation velocities are generally only possible for young inflated planets which have yet to fully contract (Baraffe et al. 2003). However, the Snellen et al. (2014) result demonstrated the feasibility of using emission or absorption profiles to quantify rotational velocities in exoplanet atmospheres. Not long after, studies by Loudén & Wheatley (2015) and Brogi et al. (2016) were able to constrain the rotational velocities in the atmosphere of HD 189733 b and found them to be consistent with the tidally-locked value of ≈ 2.7 km s $^{-1}$.

Despite the relative paucity of clear velocity measurements in hot planet atmospheres, these signatures are beginning to be teased apart by detailed examination of transmission spectra and the application of more sophisticated simulations. Flowers et al. (2019) used a suite of 3D GCMs coupled with a 1D radiative transfer code to constrain the day-to-night side wind speed and equatorial rotational velocity of HD 189733 b. Wyttenbach et al. (2020) included rotational broadening in

their detailed analysis of the Balmer line transmission spectra for KELT-9 b, showing that the profile shapes are consistent with the tidally locked equatorial rotational velocity. Ehrenreich et al. (2020) demonstrated an unprecedented level of precision in measuring the velocity centroids of individual absorption profiles for the hot Jupiter WASP-76 b and found that the highly blue-shifted absorption on the trailing limb of the planet can be explained by a combination of winds and rotation. Finally, the most comprehensive application of velocity flows in modeling a transmission spectrum was recently published by Seidel et al. (2019), who found large expansion velocities are necessary to explain the shape of the Na I D absorption line in HD 189733 b's atmosphere.

In the present manuscript we focus on transmission spectroscopy of the Balmer lines H α and H β in the atmosphere of the ultra-hot Jupiter (UHJ) WASP-33 b (Collier Cameron et al. 2010). WASP-33 b has an equilibrium temperature of $T_{\text{eq}} \approx 2750$ K and is a known pulsator with pulsation periods of ≈ 1 hour (Herrero et al. 2011; von Essen et al. 2014). It has recently joined the growing list of hot Jupiters and UHJs with atomic detections of their atmospheres (Yan et al. 2019; Nugroho et al. 2020a). We present the first detection of the Balmer lines in WASP-33 b's atmosphere and discuss in detail how measurements of the H α centroids in the transmission spectra, especially those during ingress and egress of the transit, reveal details about rotational velocities in the planet's thermosphere.

2. ATMOSPHERIC VELOCITIES FROM TIME-SERIES TRANSMISSION SPECTRA

The average transmission spectrum, or equivalent cross correlation profile (Brogi et al. 2016; Hoeijmakers et al. 2018), can provide information on the broadening mechanisms responsible for the width of the line profile (e.g., Loudén & Wheatley 2015; Allart et al. 2018, 2019; Cauley et al. 2019a) and can also reveal the net blue-shift of a day-to-night side wind (e.g., Snellen et al. 2010; Wyttenbach et al. 2015; Casasayas-Barris et al. 2019; Bourrier et al. 2020). However, most broadening mechanisms (thermal, hydrodynamic expansion, rotation, and jets) are degenerate to some degree and thus it is difficult to disentangle them using only the shape of the average in-transit absorption.

Time-series measurements of atmospheric absorption provide a means to break this degeneracy. Assuming a spherically symmetric atmosphere, both thermal broadening and atmospheric expansion produce symmetric broadening effects on the planet's transmission spectrum regardless of when during transit the planet is observed. Rotation and, to a lesser degree, jets produce an

asymmetric broadening effect during ingress and egress where, assuming the planet’s spin axis is perpendicular to the plane of its orbit, only one hemisphere dominates the transmission spectrum. We illustrate this with a cartoon in Figure 1 (see also Figures 1, 19, or 5 of [Louden & Wheatley 2015](#); [Cauley et al. 2017](#); [Flowers et al. 2019](#), respectively). We also show the difference between velocity centroids produced by atmospheric expansion, rotation, and jets in Figure 2 for the case of WASP-33 b (see Section 5 for a description of the models). For the rotation case, the velocity centroids of the transmission spectrum are blue- or red-shifted depending on which hemisphere produces the absorption. This effect was first explored by [Miller-Ricci Kempton & Rauscher \(2012\)](#), see their Figure 8) who showed that such ingress and egress velocity shifts should be detectable for hot Jupiter atmospheres.

Until recently time-resolved measurements of transmission spectrum centroids were difficult to obtain due to the mechanical and thermal instabilities inherent to non-climate controlled echelle spectrographs. As the stability and precision of high-resolution spectrographs has improved, it has become more feasible to collect high signal-to-noise transmission spectra as a function of time throughout a transit. The most spectacular example of this technique was presented by [Ehrenreich et al. \(2020\)](#) who used the ESPRESSO spectrograph to measure the velocity centroids of Fe I absorption in the atmosphere of WASP-76 b at a cadence of $\approx 6 - 7$ minutes. Using PEPSI on the LBT, we were able to measure the velocity centroids of the $H\alpha$ absorption in the atmosphere of KELT-9 b at a ≈ 5 minute cadence ([Cauley et al. 2019a](#)).

We adopt an empirical approach to determining the velocities of our $H\alpha$ transmission spectra. In other words, we do not assume a functional form for the shape of the lines and instead measure the velocities directly from the $H\alpha$ line profiles. The metric we use is the same as that defined in [Cauley et al. \(2017\)](#):

$$v_{H\alpha} = \frac{\sum_{v=-30}^{+30} v(1 - F(v))^2}{\sum_{v=-30}^{+30} (1 - F(v))^2} \quad (1)$$

where $F(v)$ is the normalized flux in the transmission spectrum at velocity v . Uncertainties for $v_{H\alpha}$ are estimated from the weighting function. First we sort the weighting function $(1 - F(v))^2$ from largest to smallest and, beginning with the largest values, we sum the function until 68% of the total has been reached. We then calculate the standard deviation of these velocities and take that value as the 1σ uncertainty on $v_{H\alpha}$. Thus broader profiles have larger uncertainties. We also discuss additional uncertainties on the measured veloci-

ties in Section 5.2, which are similar in magnitude to the empirical uncertainties. The flux-weighted velocity measurement ensures that the deepest portions of the line profile dominate the centroid determination. In general, using $v_{H\alpha}$ results in similar velocity centroids compared with, for example, fitting a Gaussian to the line profile. However when the line is asymmetric, $v_{H\alpha}$ often does a better job of finding the velocity associated with the region of greatest absorption since the profile morphology is not strictly Gaussian. Equation 1 is used to calculate the model velocities in Figure 2. We will return to the $v_{H\alpha}$ measurements of the data in Section 5.2.

3. OBSERVATIONS AND DATA REDUCTION

We observed a single transit of WASP-33 b on UT 2019-11-17 using the PEPSI ([Strassmeier et al. 2015](#)) spectrograph on the Large Binocular Telescope (LBT). The observations began at UT 01:02 and ended at UT 11:19, resulting in ≈ 4.75 hours of pre-transit exposures, ≈ 2.0 hours of post-transit exposures, and the entire ≈ 2.8 hour transit.

PEPSI was used in its $R \approx 50,000$ mode and with cross dispersers (CD) III (blue arm) and V (red arm) simultaneously. The wavelength coverage was 4750–5430 Å in the blue arm and 6230–7430 Å in the red arm. The spectra were collected with a constant signal-to-noise of 210 pixel^{-1} in the continuum controlled by a photon counter. The use of the photon counter results in slightly different exposure times for each spectrum, which ranged from ≈ 5 minutes to ≈ 10 minutes depending on airmass and seeing. A total of 82 spectra were collected in both the red and blue arms, including 26 in-transit spectra and 56 out-of-transit spectra.

The PEPSI data reduction routines follow standard high-resolution extraction procedures. Briefly, the individual science images are bias subtracted, flat fielded, and then optimally extracted. The extracted spectra are normalized using a spline fit to the continuum and corrected for the Earth’s barycentric motion at the time of the observation. We also correct for the system velocity in Table 1 to place the spectra in the rest frame of the star. More details on PEPSI data reduction can be found in [Strassmeier et al. \(2018\)](#) and [Cauley et al. \(2019a\)](#).

There are numerous telluric H_2O lines in the spectrum near $H\alpha$ which, if not accounted for, can contribute noise and extraneous features to the transmission spectrum. We used the telluric modeling procedure *Molecfit* ([Kausch et al. 2015](#)) to approximate the telluric spectrum observed for the A0 spectroscopic standard star HD 89239. We then fit the telluric model to each individual WASP-33 spectrum by scaling and shift-

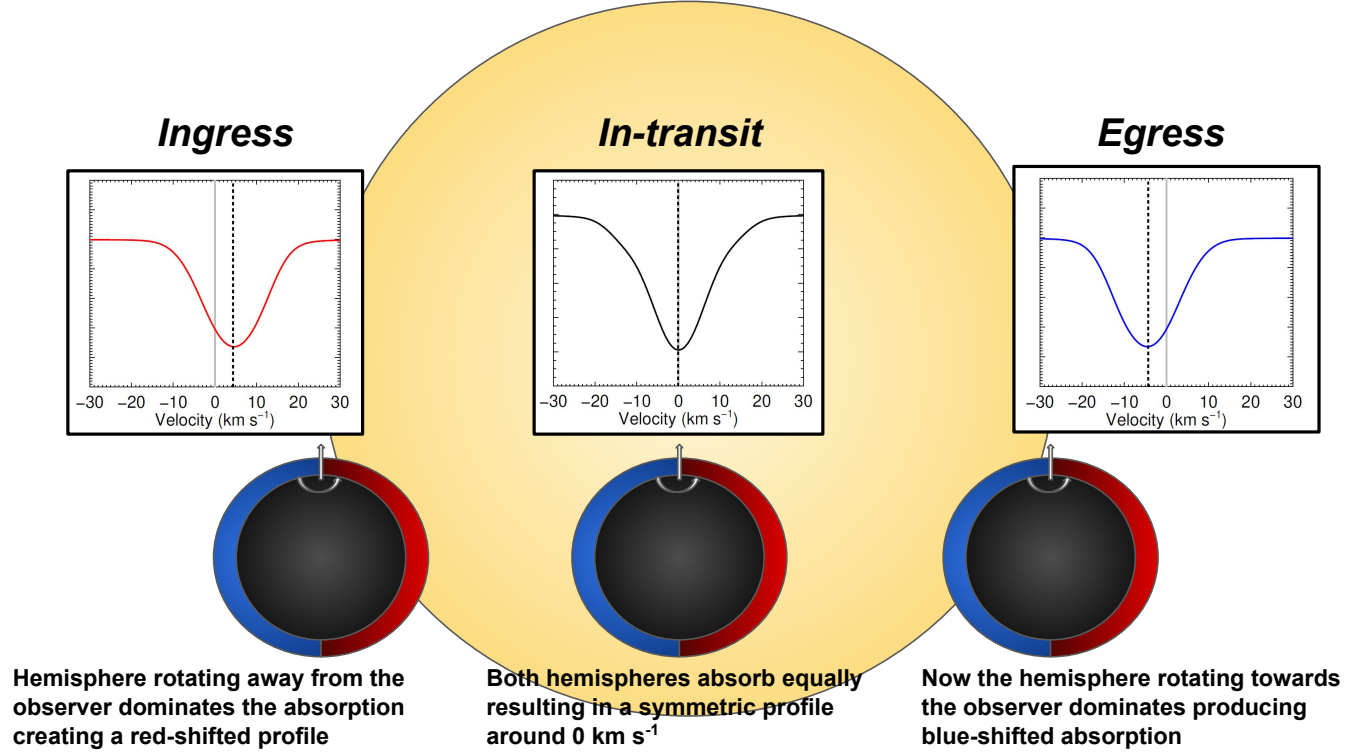


Figure 1. Demonstration of how a rotating atmosphere produces red and blue-shifted transmission spectra at various transit times. Upon ingress, the planetary hemisphere rotating away from the observer dominates the transmission spectrum resulting in a red-shifted absorption profile. The mid-transit spectrum exhibits no velocity shift but shows maximal broadening from the rotating atmosphere. Finally, the hemisphere rotating towards the observer dominates the absorption profile during egress, producing a blue-shifted transmission spectrum. Note that contributions from the star are ignored in the transmission spectrum examples.

Table 1. WASP-33 system parameters

| Parameter | Symbol | Units | Value | Reference |
|-----------------------------|------------------|--------------------|--|-----------|
| (1) | (2) | (3) | (4) | (5) |
| Stellar mass | M_* | M_\odot | $1.561^{+0.045}_{-0.079}$ | 1 |
| Stellar radius | R_* | R_\odot | $1.509^{+0.016}_{-0.027}$ | 1 |
| Stellar surface gravity | $\log g$ | cm s^{-2} | 4.3 ± 0.2 | 3 |
| Effective temperature | T_{eff} | K | 7430 ± 100 | 1 |
| Metallicity | [Fe/H] | ... | -0.1 ± 0.2 | 1 |
| Stellar rotational velocity | $v \sin i$ | km s^{-1} | $86.63^{+0.37}_{-0.32}$ | 2 |
| Spin-orbit alignment angle | λ | degrees | $-109.29^{+0.20}_{-0.17}$ | This work |
| Orbital period | P_{orb} | days | 1.2198669 ± 0.0000012 | 3 |
| Semi-major axis | a | AU | 0.02390 ± 0.00063 | 4 |
| Planetary mass | M_p | M_J | 2.16 ± 0.20 | 1 |
| Planetary radius | R_p | R_J | $1.679^{+0.019}_{-0.030}$ | 6 |
| Orbital velocity | K_p | km s^{-1} | 231 ± 3 | 5 |
| Mid-transit time | T_0 | JD | $2458804.829075^{+0.00051}_{-0.00047}$ | This work |
| Transit duration | T_{14} | hours | $2.7896^{+0.0039}_{-0.0037}$ | This work |
| System velocity | γ | km s^{-1} | 4.63 ± 0.04 | This work |

References—1 = Lehmann et al. (2015); 2 = Johnson et al. (2015); 3 = Collier Cameron et al. (2010); 4 = Chakrabarty & Sengupta (2019) 5 = Yan et al. (2019); 6 = Turner et al. (2016)

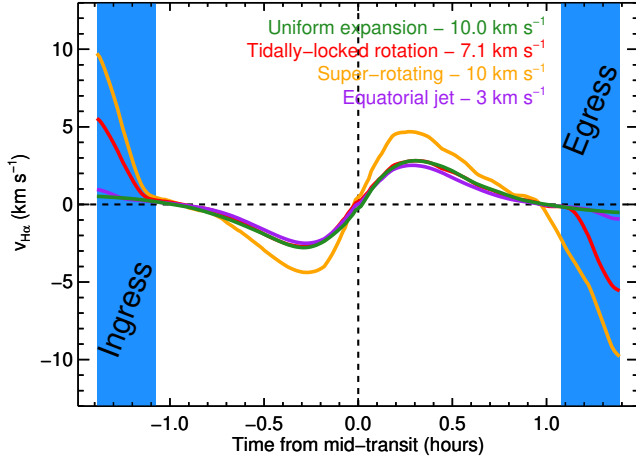


Figure 2. Examples of model velocity signatures for WASP-33 b. The uniformly expanding atmosphere (green line) shows no velocity shifts during ingress or egress due to the symmetric nature of the velocity profile. The rotating atmospheres show red-shifted absorption profiles upon ingress and blue-shifted profiles upon egress. Since the jet is confined to equatorial latitudes the velocity shift is weaker than in the rotating atmosphere case. Note that the non-zero velocities between ingress and egress are a result of the planet’s atmosphere absorbing different portions of the stellar $H\alpha$ line profile, producing slightly asymmetric absorption profiles. This occurs independently of the broadening mechanism.

ing the telluric model to match the observed telluric line depths. We then divide the best-fit model out of the stellar spectrum to produce a cleaned region surrounding $H\alpha$. We show a typical telluric model fit and removal in Figure 3. The telluric lines are removed down to the noise level in an individual spectrum.

4. TRANSMISSION SPECTRUM ANALYSIS

Here we focus on the identification of $H\alpha$ and $H\beta$ absorption in the atmosphere of WASP-33 b. The transmission spectrum extraction is complicated by two factors: 1. WASP-33 is a known δ -Scuti star and the spectral lines can be distorted by periodic pulsations in velocity space; 2. WASP-33 b is nodally precessing and thus the transit chord is variable in time. We discuss our treatment of both in the following subsections.

4.1. Determining the transit chord

WASP-33 b is nodally precessing at a rate of $d\Omega/dt = 0.4269 \pm 0.0051 \text{ deg yr}^{-1}$ (Iorio 2011; Johnson et al. 2015; Watanabe et al. 2020) which results in a variable transit chord across the star. Thus in order to accurately correct the transmission spectrum for the effects of the occulted stellar surface (i.e., center-to-limb variations and the Rossiter-McLaughlin effect), up-to-date transit parameters need to be derived from the most current tran-

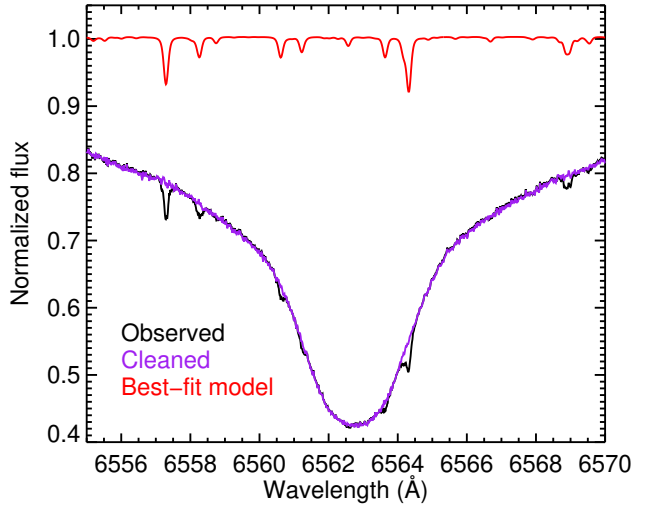


Figure 3. Example of the telluric removal procedure near $H\alpha$ for a single WASP-33 exposure. The best-fit telluric model (red spectrum) removes the observed telluric lines down to the noise level.

sit data, ideally the data from which the transmission spectrum is being extracted.

We adopt an analytical framework to model the Doppler tomography (DT) signal. In this framework, the planet DT signal is a Gaussian perturbation of the stellar line profile (Hirano et al. 2011). Line profile extraction and DT modeling are described in details in Wang et al. (2018). The modeling parameters are the impact parameter, projected spin-orbit alignment angle, projected rotational velocity, quadratic limb darkening parameters, planet-star radius ratio, systemic velocity, and the mid-transit time.

One difficulty in extracting line profiles for WASP-33 is its pulsation as a δ -Scuti variable star. We apply a customized Fourier filter to remove the pulsation signal. A similar strategy was adopted in previous works (Johnson et al. 2015; Watanabe et al. 2020). The difference is that we use a series of inverse normalized Gaussian profiles to mask out the strongest pulsation frequencies in the Fourier space until the DT signal stands out clearly. This approach minimizes the “ringing” effect as seen in previous works thanks to the apodizing Gaussian profiles.

We give the modeled transit parameters from our analysis in Table 1. We display maps of the DT signal, the associated model, and the model residuals in Figure 4. We adopt the mid-transit time, spin-orbit alignment angle, transit duration, and system velocity from our DT analysis given their importance in creating the transmission spectrum and the fact that these values change over time due to the planet’s precession. All of the other

WASP-33 system parameters are taken from the literature.

4.2. Constructing the transmission spectra

We calculate the individual transmission spectra by dividing each stellar spectrum by the mean out-of-transit stellar spectrum, which we will refer to as the “master-out”. All of the out-of-transit spectra have the same signal-to-noise due to the use of the photon counter. Thus we do not exclude any spectra from the master-out spectrum based on quality. We do, however, only use spectra with observations midpoint times of $|T_i| > 2.0$ hours in order to avoid using spectra near the transit as out-of-transit comparisons. We determine the time from mid-transit for each exposure using the values of T_0 and T_{14} derived in Section 4.1. The final master-out is composed of 46 out-of-transit spectra.

Each in-transit transmission spectrum needs to be corrected for the distortions caused by the occulted portion of the stellar disk during that observation. The primary effects are center-to-limb variations (CLVs) in the spectral line and the Rossiter-McLaughlin (RM) distortion caused by occultation of a piece of the rotating stellar disk (e.g., Czesla et al. 2015; Yan et al. 2017; Cauley et al. 2019a). To model these effects we follow the same procedure presented in Yan & Henning (2018) and Cauley et al. (2018, 2019a). For each spectral line of interest, in this case $H\alpha$ and $H\beta$ we create synthetic spectra using *Spectroscopy Made Easy* (Piskunov & Valenti 2017) and the stellar parameters in Table 1. We generate spectra at 25 different μ -angles to account for CLVs in the spectral lines.

We then generate a grid representing the stellar disk. Each element in the grid has dimensions $0.01R_* \times 0.01R_*$. We assign a spectrum to each grid point by shifting that spectrum according to the local rotational velocity of that grid location and applying the wavelength-dependent limb-darkening derived from the synthetic spectra calculated at the various μ -angles. The synthetic out-of-transit spectrum is then the sum of the spectra for all of the grid points on the stellar disk. We use EXOFAST (Eastman et al. 2013) to calculate the planet positions on the stellar disk to generate model CLV+RM profiles for the midpoint of each exposure. We divide these model profiles out of the transmission spectra to remove the CLV+RM features. It is worth highlighting that the CLV+RM profiles only interfere with the planet’s absorption signature when the absorption profile overlaps the CLV+RM profile in velocity space. Thus if these signatures are not modeled explicitly then it is acceptable to simply throw out the in-transit exposures for which the planet’s line-of-sight

velocity intersects the local occulted rotational velocity (e.g., Ehrenreich et al. 2020; Wyttenbach et al. 2020).

We do not consider an increase in magnitude of the CLV+RM profiles due to an increased effective planet radius in a given spectral line, as suggested by Yan & Henning (2018). There are two reasons for this. The first is that we see no consistent evidence at $H\alpha$ or $H\beta$ for an amplified CLV+RM effect, although a few transmission spectra exhibit larger than expected signals. The second reason is that absorption by the planet’s atmosphere only increases the magnitude of the CLV+RM profile when the line-of-sight velocity of the planet overlaps significantly with the local occulted rotation velocity. This is because the star effectively “sees” the larger planetary radius at the velocity in the spectrum at which the atoms are absorbing. As we will discuss, the exposures during which the planet’s velocity overlaps the local stellar rotational velocity (middle portion of the transit in Figure 5) show anomalously weak absorption and are not included in much of our analysis. Thus we do not consider the enhanced CLV+RM effect since the exposures which should most strongly be affected show marginal planetary absorption.

We show the spectral time-series maps of the $H\alpha$ and $H\beta$ transmission spectrum, S_i/S_{out} , in Figure 5. The stellar pulsation signal is visible in the pre-transit data as the dark and light stripes that extend from approximately $-v\sin i$ to $+v\sin i$, which are marked with the vertical green lines. We show the transit start and end times T_1 and T_4 with the horizontal purple lines. We also show the planet’s line-of-sight velocity, calculated using the value of K_p from Table 1, with the blue line. Absorption in both $H\alpha$ and $H\beta$ is visible during the transit and closely tracks the planet’s velocity. There is a noticeable lack of absorption during the central portion of the transit. Although the absorption is expected to be weaker here due to the planet’s velocity moving across the deepest section of the local stellar $H\alpha$ and $H\beta$ lines, our models, which we discuss in the next section, cannot account for a complete absence of absorption. We note that a similar effect is seen by Casasayas-Barris et al. (2019) for the UHJ KELT-20 b.

The same anomaly is present in Figure 6, which shows the equivalent width of the Balmer line transmission spectra as a function of time, where the absorption disappears entirely near mid-transit and is weaker during the second half of the transit compared with the first half. One possible explanation for the weaker than expected absorption is the overlap of the planet’s absorption profile with a pulse profile. Given the pulse model results in the next section, it seems unlikely that a pulse profile could entirely mask the absorption during the

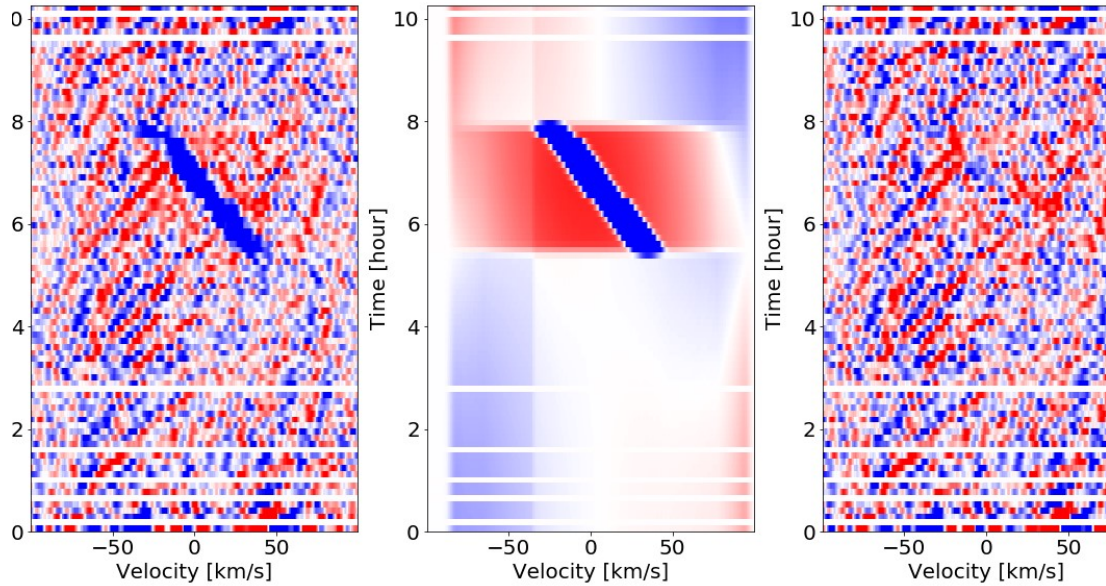


Figure 4. **Left:** Fourier-filtered residual map after subtracting the median line profile. The planet “Doppler shadow” is the diagonal blue track running from the bottom-right to the top-left. **Middle:** Modeled DT signal. **Right:** difference of the two maps on the left and middle panel.

second half of the transit. We defer a more detailed exploration of the interplay between the pulse profiles and absorption depths to future work.

We present the average in-transit Balmer line transmission spectra in Figure 7. We only include the spectra taken between $-1.0 \text{ hours} \leq t_i \leq -0.56 \text{ hours}$ in the average due to the lack of absorption in the middle portion of the transit and the weaker absorption during the second half of the transit. This resulted in a total of 5 in-transit spectra. Before averaging we shift the selected spectra into the rest-frame of the planet using the orbital and transit parameters from Table 1. We include plots of the individual transmission spectra in the planet’s rest frame in Section 7. We list Gaussian fit parameters to the average transmission spectra in Table 2. Note that the measured blue-shifted velocity offset could be partially due to the uncertainty in the transit midpoint timing (see subsection 5.1.1).

We measure the absorption in the average transmission spectra using the equivalent width integrated from -100 km s^{-1} to $+100 \text{ km s}^{-1}$. These values are listed in column 5 in Table 2: the $\text{H}\alpha$ absorption is detected at $\approx 46\sigma$ and the $\text{H}\beta$ absorption is detected at $\approx 12\sigma$. The absorption is significant and represents the first detection of the Balmer lines in WASP-33 b’s atmosphere.

4.3. Stellar pulsations and their effect on the transmission spectrum

Table 2. Balmer line Gaussian fit parameters and absorption measurements

| | Contrast | FWHM | v_0 | W_λ |
|------------------|------------------------|------------------------|------------------------|--------------------------|
| Line | (%) | (km s^{-1}) | (km s^{-1}) | ($\text{m}\text{\AA}$) |
| (1) | (2) | (3) | (4) | (5) |
| $\text{H}\alpha$ | $1.68^{+0.02}_{-0.02}$ | $45.4^{+0.7}_{-0.8}$ | $-4.5^{+0.3}_{-0.3}$ | 17.5 ± 0.4 |
| $\text{H}\beta$ | $1.02^{+0.05}_{-0.05}$ | $33.0^{+2.5}_{-2.4}$ | $-1.7^{+0.8}_{-0.8}$ | 12.2 ± 0.4 |

WASP-33 is a well known pulsator (e.g., Collier Cameron et al. 2010; Herrero et al. 2011; von Essen et al. 2014, 2020) with pulsation periods of ≈ 1 hour. Pulsations in spectroscopic data can be seen as bumps that, in WASP-33’s case, move between $-v \sin i$ and $+v \sin i$ in velocity space across the line profile as a function of time (e.g., Johnson et al. 2015). In our Balmer line time series this is most clearly seen in the pre-transit spectra in Figure 5 as the diagonal bright and dark bands. Since the pulsation features overlap with the planet’s line-of-sight velocity and have periods on the order of the transit duration, it is possible for the pulsations to distort or contaminate the transmission spectrum.

In order to attempt to predict the in-transit pulse signal and remove it from the transmission spectra, we

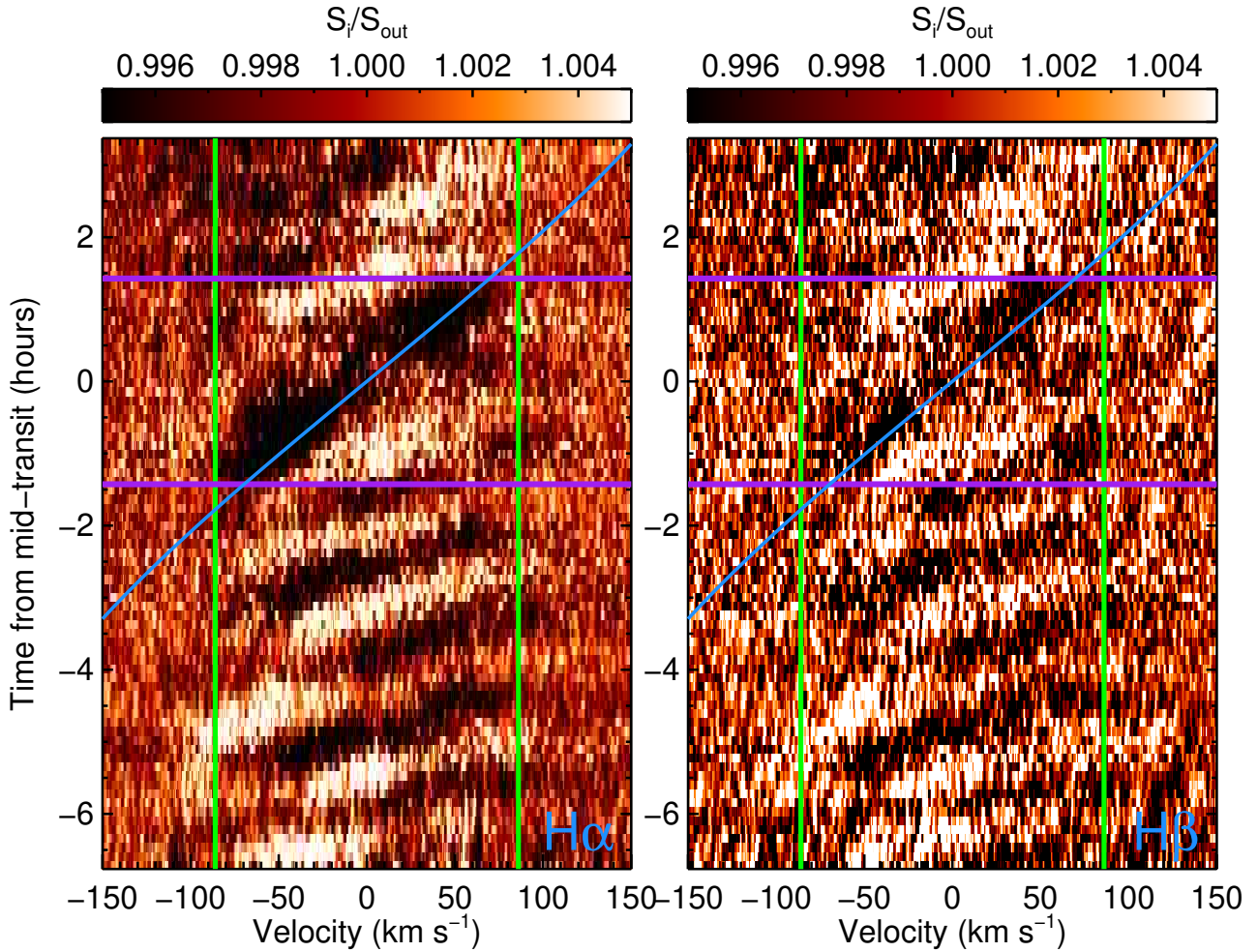


Figure 5. Spectral map of the $H\alpha$ and $H\beta$ transmission spectra in the stellar rest frame for the entire night. The spectra have been interpolated onto an evenly spaced time vector for display purposes which produces some of the smearing near the beginning and end of the night when exposures were longer on average. The transit contact points T_1 and T_4 are shown with horizontal purple lines. The star’s $\pm v \sin i$ value is marked with the vertical green lines. The planet’s line-of-sight velocity is shown with the blue line. There is a clear $H\alpha$ signature which moves along the planet’s velocity for the duration of the transit. The $H\beta$ absorption is weaker but still present at the expected velocities. Note the pulsation stripes visible in the pre-transit data in both lines.

modeled the pulses as two periodic pairs of Gaussians where each pair has a positive and negative amplitude Gaussian with a fixed velocity separation. The model also includes the FWHM of the pulses, the minimum and maximum velocities of the pulses, and the rate at which the pulses traverse the stellar disk. We use a custom MCMC routine based on the algorithm in [Goodman & Weare \(2010\)](#) (see also [Foreman-Mackey et al. 2013](#)) to find the maximum likelihood fit for the pulse model. We assume uniform priors for all parameters and run the MCMC chains for 10^5 steps with 10^2 walkers per chain. We choose the most-likely parameters as the median values of the marginalized posterior distributions.

The most-likely pulse model for $H\alpha$ is shown in [Figure 8](#) and [Figure 9](#). In general, the pulse model is a good approximation to the observed pulse structure in

the pre-transit $H\alpha$ spectra. However, there are some noticeable discrepancies, for example, at $t = -368$ minutes and $t = -170$ minutes where the amplitude and phase of the observed pulse is not predicted by the model. Thus although the model is useful in understanding the structure of the pulse spectra we do not consider it accurate enough to predict the in-transit pulse signal, which is more difficult to quantify due to its overlap with the planetary features. Furthermore, it is unclear exactly what effect the transit itself has on the pulsation signature, which would not be predicted by our simple model of the out-of-transit pulsations. Thus we choose to forego removal of the in-transit pulse signature given the uncertainties involved.

Since we choose not to remove the modeled pulse signal from the data, and we are primarily concerned

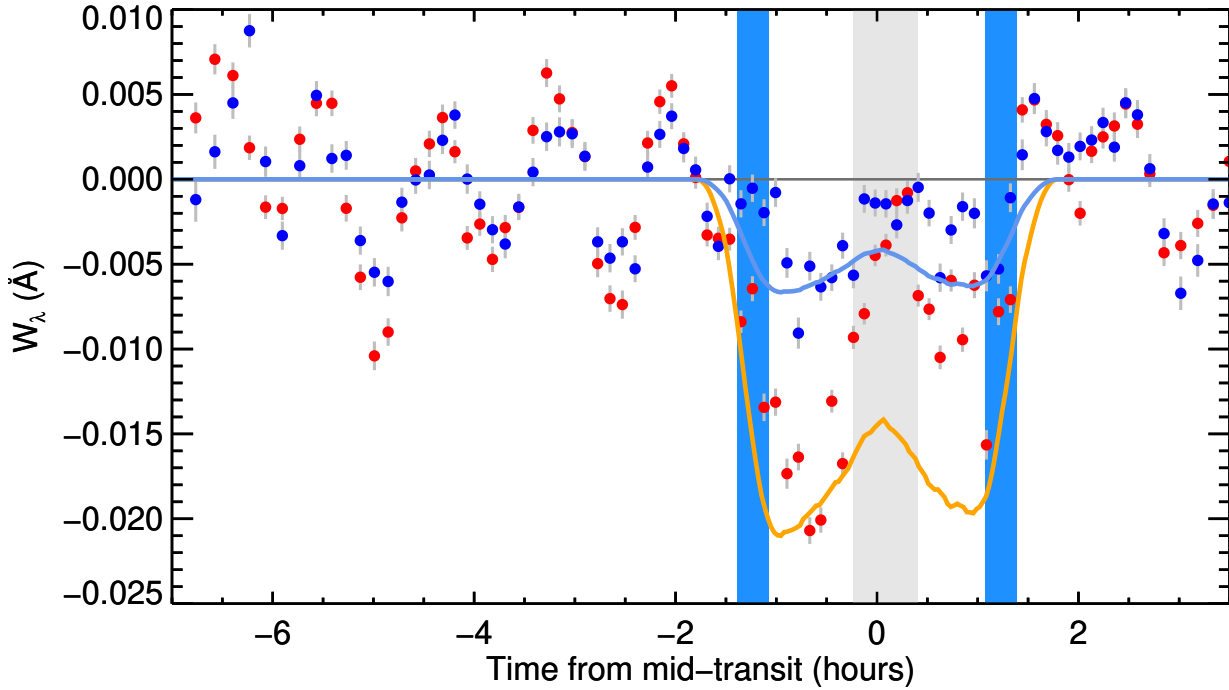


Figure 6. Equivalent width time-series of the individual Balmer line transmission spectra. The $H\alpha$ data is plotted with red circles and the $H\beta$ data is shown with blue circles. The ingress and egress portions of the transit are the light blue filled regions. The filled gray region represents where the planet’s absorption signal overlaps with the local RM signal from the stellar surface. The absorption models (solid blue and orange lines) are calculated using the best-fit parameters from the transmission spectrum fitting in [subsubsection 5.1.3](#). There is asymmetry in the transit with the first half absorption being much stronger than the second half. Note the pulsation signal that is visible in the pre-transit data.

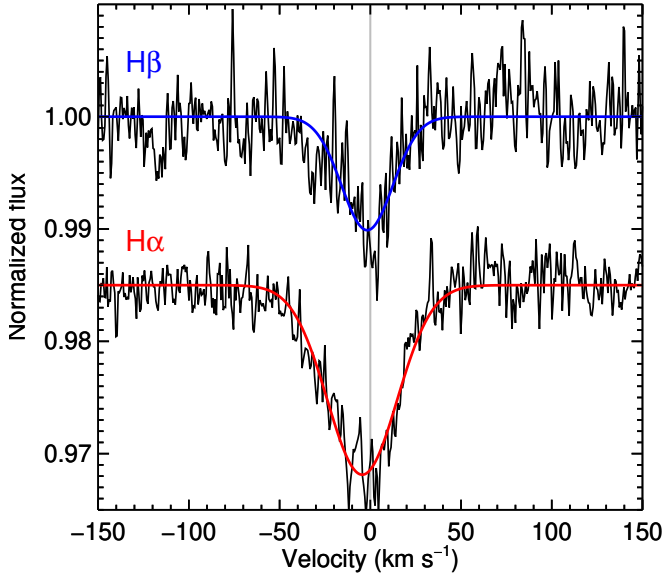


Figure 7. Average transmission spectra for $H\beta$ (top) and $H\alpha$ (bottom) with best-fit Gaussian profiles over-plotted in blue and red, respectively. There is a significant blue-shift in both lines, which we discuss in [subsubsection 5.1.3](#).

with measuring the centroid velocities of the transmission spectra in the rest frame of the planet, we need to understand how the pulse profiles can perturb the centroid measurements from [Equation 1](#). To explore this we simulate how various modeled pulse profiles change the velocity centroid of a simulated transmission spectrum. We generate the transmission spectrum using the models in [Section 5](#) and choose the parameters so as to approximate the morphology of the average in-transit $H\alpha$ transmission spectrum from [Section 3](#) in the rest frame of the planet. We choose three representative pulse profiles from [Figure 9](#), specifically the profiles at $t = -358$, $t = -296$, and $t = -233$ minutes, as the perturbing pulses. We then shift the pulse profiles across the transmission spectrum from $\Delta v = -100 \text{ km s}^{-1}$ to $+100 \text{ km s}^{-1}$, add the shifted pulse profile to the transmission spectrum, and calculate the centroid velocity $v_{H\alpha}$ of the perturbed spectrum.

We show the result of the simulation in [Figure 10](#). The maximum perturbation from the true value of $v_{H\alpha}$, which we label $v_{\text{true}} - v_i$ on the vertical axis, is $\approx 6 \text{ km s}^{-1}$; the average perturbation is $\approx 1.7 \text{ km s}^{-1}$ and the standard deviation of the perturbed velocities is 1.5

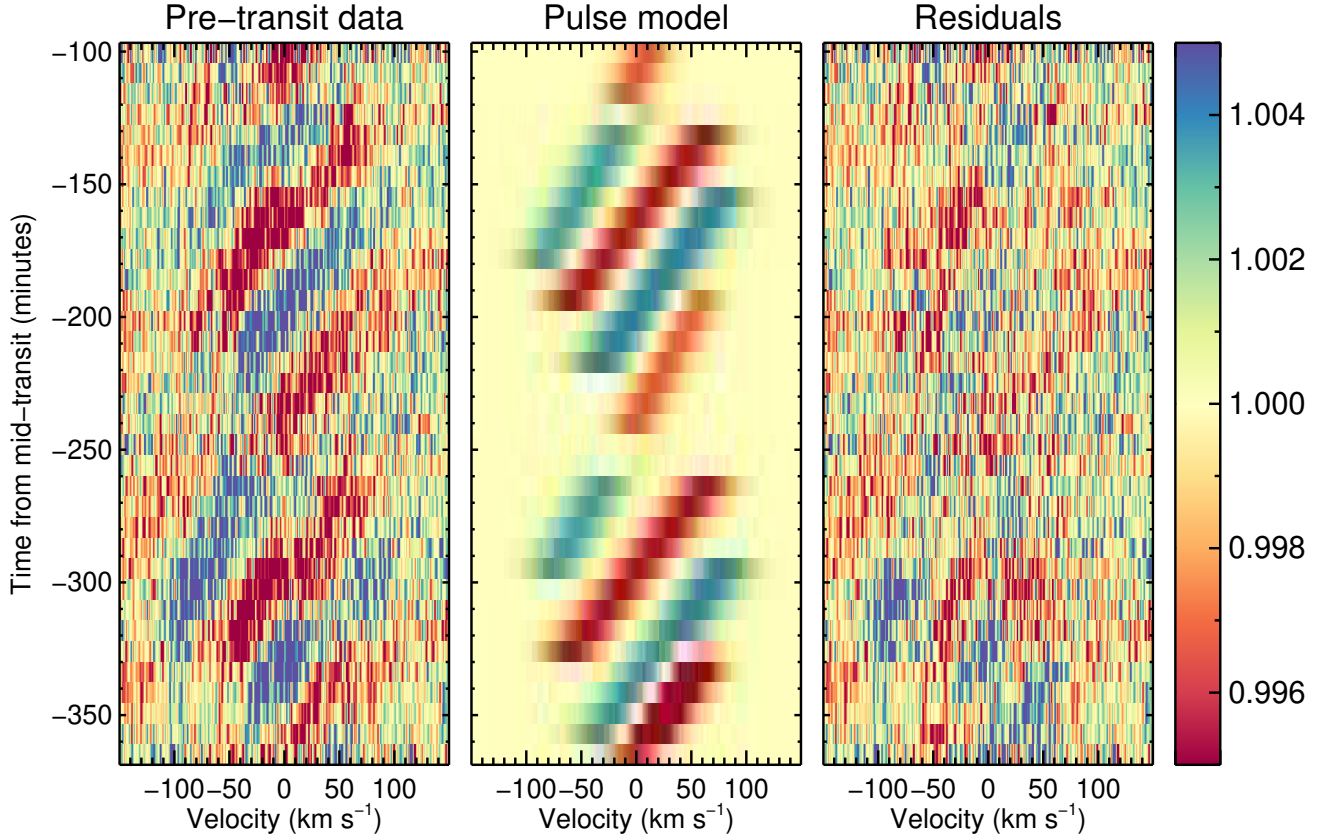


Figure 8. Maps of the pre-transit pulse signal. The pre-transit data is in the left panel and the best-fit pulse model is shown on the right. The pulse model approximately reproduces the structure of the pulses but some features are visible in the residual map.

km s^{-1} . Thus on average we expect the shape of the transmission spectra to be modified by the pulses so that the measured centroid velocities differ from the true centroid velocity by $\approx 1.7 \text{ km s}^{-1}$. In lieu of removing the in-transit pulse profiles we instead include the 1.7 km s^{-1} pulse contribution as additional uncertainty on the values of $v_{H\alpha}$ in Section 5.2.

5. ATMOSPHERIC MODELS WITH VELOCITY DYNAMICS

In order to constrain the atmospheric dynamics responsible for the profile morphologies and measured velocities in WASP-33 b’s extended atmosphere, we have developed numerical models that take into account the effects of rotation, uniform expansion, day-to-night side winds, and equatorial jets on the transmission spectrum. The structure of the models is the same as those in Cauley et al. (2019a) and we review them here. Our models are three-dimensional in the sense that we calculate the column densities and optical depth vectors through a chord of the atmosphere

using a three-dimensional array but the radiative transfer is performed on the collapsed 2-D atmosphere. Thus we do not include asymmetric geometry effects such as a hotter and more extended westward planetary limb (e.g., Flowers et al. 2019).

We model the planetary atmosphere on the same discrete grid used to simulate the stellar CLV+RM profiles. The grid points have size $0.01R_* \times 0.01R_*$ which for WASP-33 b equates to $0.087R_p \times 0.087R_p$. The atmosphere is spherically symmetric and of uniform density and is parameterized by r (in units of R_p), the distance above the optical planetary radius R_p , and the number density n (in units of cm^{-3}). While the assumption of uniform density is not strictly correct, sophisticated models of the $n = 2$ electronic level number density in hot and ultra-hot Jupiter atmospheres suggests that it varies slowly with decreasing pressure in the thermosphere where the Balmer lines form (Huang et al. 2017; García Muñoz & Schneider 2019). We initially construct the atmosphere in 3D and then collapse the grid into the

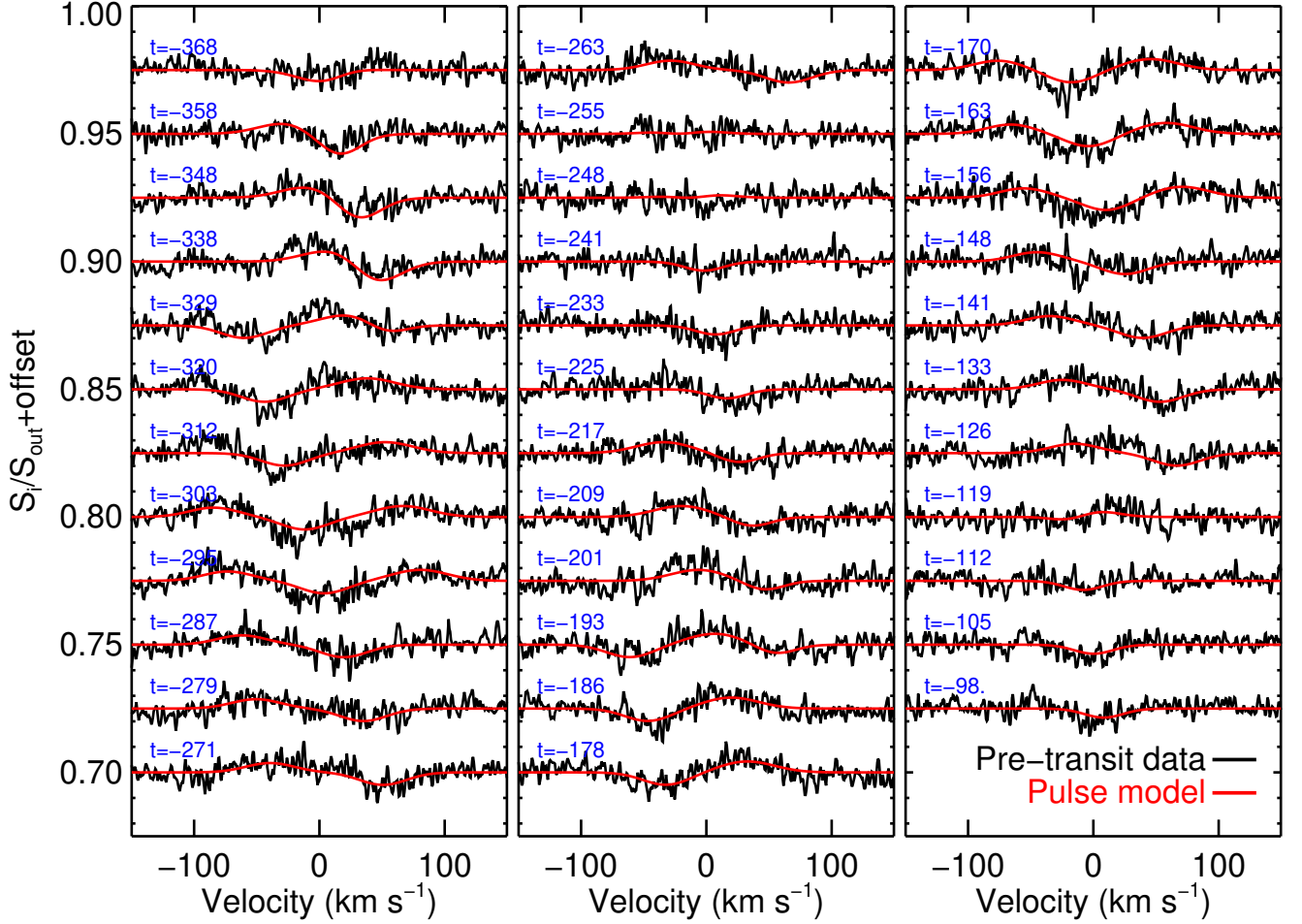


Figure 9. Individual pre-transit spectra (black) and the most-likely pulse model spectra (red) for $H\alpha$. The time from mid-transit in minutes is given in blue. Overall, the pulse model provides a good approximation to the individual pulse spectra.

plane perpendicular to the line-of-sight between the observer and the star so that the atmosphere grid is now in units of column density (cm^{-2}).

We compute the transmission spectrum $S_T(t)$ at time t in the transit by looping through the atmosphere and extinguishing the stellar intensity at each atmospheric grid point $I_*^i(t)$ by the optical depth τ_i through the same grid point. We do not consider multiple scatterings in the atmosphere. We also sum the stellar grid points that are not occulted by the planet nor absorbed by the atmosphere and call this spectrum $I_*^{\text{in}}(t)$. We then add $I_*^{\text{in}}(t)$ to the spectrum absorbed by the planet’s atmosphere and divide by the out-of-transit spectrum I_*^{out} , which has been corrected for the CLV+RM profile $I_{\text{tran}}(t)$. Algebraically this can be written as

$$S_T(t) = \frac{I_*^{\text{in}}(t) + \sum_i I_*^i(t) e^{-\tau_i}}{I_*^{\text{out}} - I_{\text{tran}}(t)}. \quad (2)$$

Before the stellar spectrum is extinguished we shift the optical depth vector, which we model as a Voigt profile with Gaussian broadening component v_t and Lorentzian component v_{Lor} , by the velocity of the local grid point. We assume a uniform day-to-night side wind speed v_{wind} in the atmosphere which requires a single-valued velocity shift of the optical depth at each grid point. Note that in reality non-uniform wind speeds result in some broadening of the line profile (Flowers et al. 2019) since the velocity dispersion is non-zero. However, rotational and thermal broadening likely dominate for UHJs like WASP-33 b.

For the case of rotation we consider the atmosphere to be rigidly rotating so that the rotation velocity v_{rot} at R_p at the equator scales linearly with distance from the rotation axis. For example, for $v_{\text{rot}} = 6.0 \text{ km s}^{-1}$ the velocity at $r = 0.5$ above the equator would be 9.0 km s^{-1} . As noted by Wyttenbach et al. (2020), the

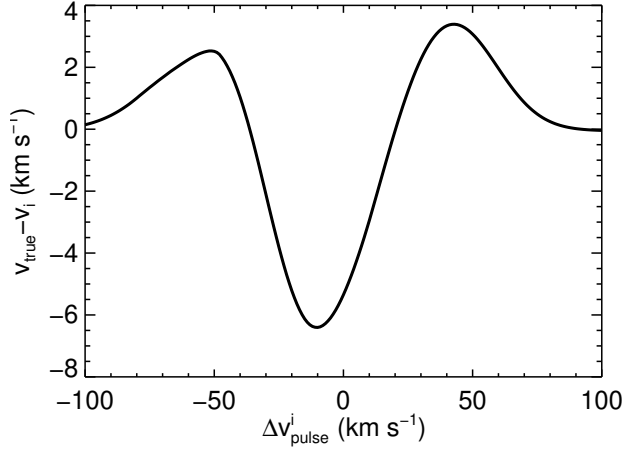


Figure 10. Difference between the true velocity centroid value v_{true} for the simulated transmission spectrum and the velocity centroid v_i for the pulse-perturbed profile for each velocity shift $\Delta v_{\text{pulse}}^i$. When the pulse peaks overlap with the atmospheric absorption the perturbation can be non-negligible. However, on average the perturbations are $\approx 2 \text{ km s}^{-1}$ in magnitude which is similar to the empirical uncertainties on the measured $v_{H\alpha}$ values.

line-of-sight velocity along any line perpendicular to the rotation axis through a 3D rigidly-rotating atmosphere is constant. Thus we can apply the rotational velocities to the 2D density grid without accounting for the velocities in the full 3D case. The column density through the atmosphere decreases as a function of r so the larger velocities contribute least to the rotational broadening compared with the smaller velocities at lower altitudes. We assume that the planet’s rotation axis is parallel to its orbital angular momentum vector.

For uniform spherical expansion, the velocity field must be treated in 3D since each grid point will have a different line-of-sight velocity depending on the angle between the grid point and the line-of-sight. This results in a broadening of the optical depth profile along any sight line through the atmosphere. Because of the need for 3D accounting in this case, we do not collapse the density array beforehand. Instead, we loop through the atmosphere and calculate the velocity shifts for each grid point and then sum the total optical depth along the sight line. Although our models are capable of modeling expanding atmospheres, the Balmer lines form at pressures where the upward velocities are expected to be on order of $\approx 1 \text{ km s}^{-1}$ (Salz et al. 2016; Wyttenbach et al. 2020). Thus uniform expansion cannot account for the velocity signature seen in Section 5.2 and we do not explore it further.

We also consider the effects of equatorial jets, which contribute to the broadening of the optical depth pro-

file. In our models we force the jets to exist between planetary latitudes of $|\theta| < 25^\circ$ and we take the jet velocity to be constant as function of latitude and altitude in the atmosphere. We assume the jet travels in the same direction as the planet’s rotation. The result of including the jet velocity is increased broadening since the jet speed is only applied to an equatorial band in the planet’s atmosphere. However, as noted in Section 2 and demonstrated in Figure 2, jets in our model produce weaker velocity shifts upon ingress or egress when compared with a rotating atmosphere of the same velocity. This is due to the jet speed being constant throughout the atmosphere and the limited latitude contribution of the jet broadening.

5.1. Modeling the Balmer line transmission spectra

Before we present the application of the models described in Section 5 to the transmission spectra, there are two details which require a more in-depth discussion given their effects on fitted model parameters.

5.1.1. Mid-transit time and line-of-sight velocity

Exoplanet transit ephemerides require frequent updates in order to refine the mid-transit time of future transits. While simultaneous high-quality photometry is the ideal method for determining transit parameters for a corresponding spectroscopic transit (e.g., Johnson et al. 2015), modeling the spectroscopic transit itself can provide important constraints on the mid-transit time which are superior to using out-of-date ephemerides.

The mid-transit time becomes critically important for measurements of the velocity offsets in transmission spectra or cross-correlation measurements: changing the mid-transit time by a few minutes can alter the planet’s inferred line of sight velocity by $\sim 1 - 2 \text{ km s}^{-1}$ thus shifting the measured velocity of the transmission spectrum in the frame of the planet. This can lead to spurious, or inaccurate, measurements of a day-to-night side wind.

For WASP-33 b we find that the in-transit line-of-sight velocity of the planet changes by $\approx 0.8 \text{ km s}^{-1}$ per minute of difference in the mid-transit time. For example, if the true mid-transit time differs from our modeled mid-transit time by ≈ 3 minutes then the magnitude of the line-of-sight velocity change will be $\approx 2.5 \text{ km s}^{-1}$.

Although this uncertainty in the planet’s line-of-sight velocity does not affect the transmission spectrum itself, it translates directly as an uncertainty in the velocity shift of the transmission spectra into the rest frame of the planet. In turn, this uncertainty propagates into model parameters which estimate any overall velocity shifts in the transmission spectrum. Note that the mid-transit time uncertainty does not affect the structure of

the $v_{H\alpha}$ time series since it produces an approximately constant shift for all in-transit spectra. For our models the affected parameter is the wind velocity v_{wind} . The statistical uncertainty on our derived mid-transit time (see Table 1) is ≈ 1 minute but this is likely an underestimate; the actual mid-transit time uncertainty is probably closer to $\approx 3 - 4$ minutes. Thus in our final determination of v_{wind} we include an additional uncertainty of 3.0 km s^{-1} to account for the mid-transit time error.

5.1.2. Doppler smearing

High-resolution spectroscopic transit observations necessarily have exposure times on the order of minutes. The planet, however, is continuously changing its line-of-sight velocity and position on the stellar disk. Thus any observation can be approximated by averaging the instantaneous spectra sampled finely enough from the beginning to the end of the exposure. The result is an observed spectrum that has been broadened, or blurred, by the motion of the planet during the exposure, where longer exposures result in more broadening (Ridden-Harper et al. 2016; Wyttenbach et al. 2020). This is critical for transmission spectrum modeling since most models tend to simulate the spectrum at a single time, either at mid-transit or at the average mid-exposure time for the spectra which have been averaged to create the transmission spectrum. If the broadening is non-negligible models must take this effect into account by either including it explicitly, which is computationally expensive, or by approximating the effect with an applied broadening function (e.g., Wyttenbach et al. 2020).

The question arises: what is the maximum exposure time for a planet that results in negligible smearing in the observed transmission spectrum? Using our models we have tested the Doppler smearing effect for WASP-33 b for an observation with mid-exposure time of $t = -30$ minutes from mid-transit. We tested multiple exposure lengths from 5 minutes up to 45 minutes and generated instantaneous spectra at 1-minute intervals throughout the exposure. Two examples are shown in Figure 11 for exposure duration of $t_{\text{exp}} = 10$ minutes (left panel) and $t_{\text{exp}} = 30$ minutes (right panel). The mean spectrum (red line) is calculated by averaging all of the instantaneous spectra (gray lines). The mid-exposure spectrum is the instantaneous transmission spectrum at the midpoint of the exposure. Doppler smearing can be ignored when the differences between the two spectra are negligible.

While we do not derive any specific relationships for the magnitude of the effect as a function of exposure

duration, it's clear the Doppler smearing is essentially absent from the $t_{\text{exp}} = 10$ minute spectrum while it is beginning to manifest in the $t_{\text{exp}} = 30$ minute case. Since our longest observations are ≈ 10 minutes we conclude that Doppler smearing can be safely ignored in our transmission spectrum modeling described in subsection 5.1.3. This effect should be evaluated on a case-by-case basis since narrower spectral lines will be more strongly affected and planets with larger orbital velocities will experience more dramatic smearing.

5.1.3. Balmer line model results

We applied the models described in Section 5 to the average $H\alpha$ and $H\beta$ transmission spectra shown in Figure 7. For each model iteration the transmission spectra of $H\beta$ and $H\alpha$ are calculated simultaneously at the mean x and y locations on the stellar disk of the exposures included in the transmission spectrum being fit. In other words, we do not calculate a spectrum for each exposure and then average them to produce the model average transmission spectrum but rather calculate a single spectrum at the mean transit time of all exposures.

We employ the same maximum-likelihood MCMC routine referenced in Section 4.3 to find the most-likely model parameters for the Balmer line transmission spectra. We explore eight scenarios, each a subset of the simplest case which only includes thermal broadening. The model abbreviations are letters which correspond to the descriptors Thermal (T), Rotation (R), Wind (W), and Jet (J). We also test a special case, Model TWJ+R_{tl} which fixes the rotational velocity at the tidally locked value of 7.1 km s^{-1} but allows the jet velocity to vary. We then compare the fit results using the Bayesian information criterion (BIC). The potential free parameters in the model are number density n , radial extent r above $R_p = 1.0$, thermal broadening v_t , Lorentzian broadening v_{Lor} , rotational broadening v_{rot} , the day-to-night side wind velocity v_{wind} , and the equatorial jet velocity v_{jet} . In the models which do not include rotation, a day-to-night side wind, or a jet the corresponding parameter values are set equal to zero. We assume broad uniform priors for all parameter values.

Each MCMC chain is initiated with 100 independent walkers which are each run for 1500 steps. We eliminate the first 500 steps as burn-in and use the remaining samples, which we test for convergence using the Gelman-Rubin statistic, to generate 1D and 2D posteriors for the parameters. We choose the best-fit parameters by taking the median value of the marginalized 1D posteriors; we calculate $1 - \sigma$ confidence intervals as the 68% regions around the median values.

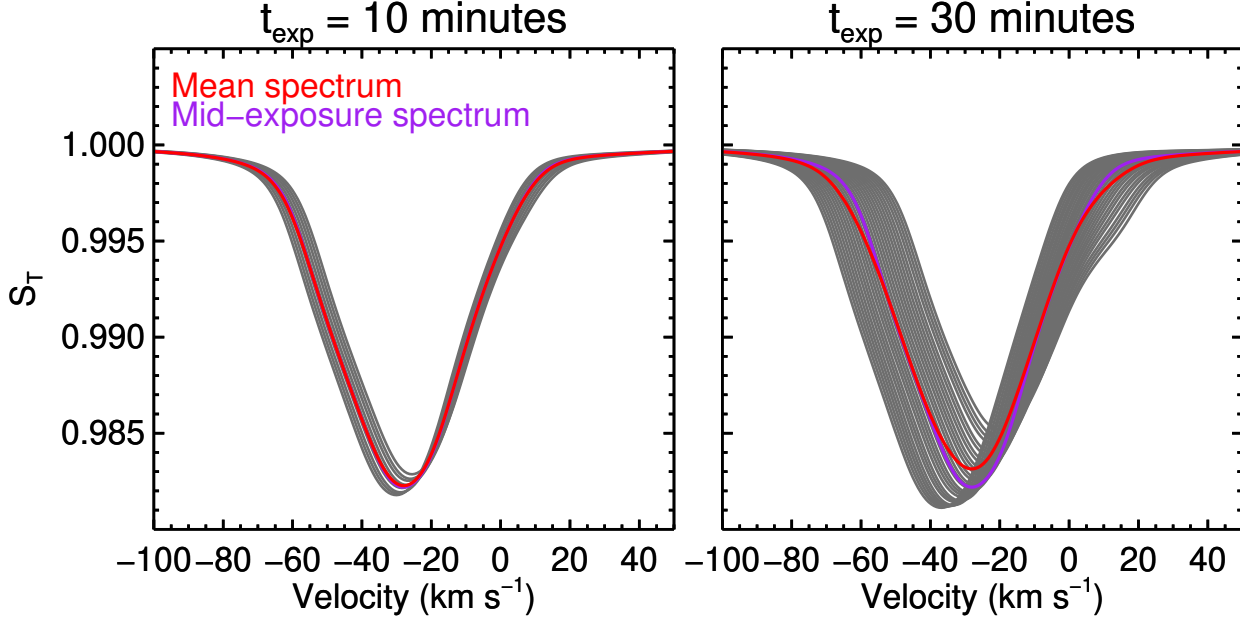


Figure 11. Examples of Doppler smearing for WASP-33 b. The left panel shows the case of a 10-minute exposure and the right panel shows a 30-minute exposure. For the 10-minute case there is very little smearing, i.e., the mean spectrum of the exposure very closely approximates the instantaneous spectrum at the time of mid-exposure. In the 30-minute example, however, the smearing effect is noticeable: the mean spectrum is broadened relative to the mid-exposure spectrum.

It is important to note that due to the finite size of the pixels in our model grid, the variable r is discrete and thus the confidence intervals determined from the marginalized posterior are not strictly accurate. They can be thought of as lower bounds on the actual confidence interval since MCMC steps with r values between pixels with values r_1 and r_2 were rejected so only values of r up to and including r_1 are realized in the posterior. We adopt a conservative confidence interval of 0.5 pixels, or $0.045R_p$, for the confidence intervals on r which are less than this.

We show the corner plot of the 1D and 2D histograms for Model TRW in Figure 12 and the results of the eight model fits in Figure 13. We list the most-likely parameters and their uncertainties in Table 3. The ΔBIC values are relative to the Thermal (T) model. It's clear upon visual inspection of the line profile fits that the models which include the day-to-night side wind are strongly favored over the models with no wind. This was foreshadowed by the Gaussian fits to the average transmission spectra which also found significant blue-shifts in the spectra. For the no-wind models the natural broadening v_{Lor} tends to be large since the MCMC is attempting to find solutions that can match the blue side of the profile. Thus the resulting v_{Lor} values are unrealistic since there is no pressure broadening at the densities and pressures

where H α forms in hot planet atmospheres (Huang et al. 2017; Wyttenbach et al. 2020; Turner et al. 2020).

Although the models which include an equatorial jet and a wind (Models TRWJ, TWJ, and TWJ+R $_{\text{tl}}$) show similar or lower BIC values, the most-likely jet velocities are likely too large to be physical (Table 3): all three jet models find a jet velocity of $\approx 19 - 20 \text{ km s}^{-1}$. GCMs currently do not explore micro- and nano-bar pressures but there is little evidence that such large jet velocities are possible even in the extreme atmosphere of UHJs (Flowers et al. 2019; Carone et al. 2020). Given the unrealistic jet values found by our models, we choose to proceed by only considering the rotation models and their explanatory power for the measured in-transit transmission spectrum velocities.

The TRW and TW models both provide better descriptions of the Balmer line transmission spectra than the purely thermal model. This is verified by their significantly lower BIC values. Including rotation gives the best description of the data: the BIC value for the TRW model is 30 points lower than the TW model, strong evidence that the TRW model is a better approximation to the atmosphere than the TW model. We conclude that incorporating rotation into the model line profiles provides a more accurate description of WASP-33 b's atmospheric physics. Our model suggests that the rotational velocity probed by the Balmer lines is $v_{\text{rot}} = 10.1^{+0.8}_{-1.0}$

km s^{-1} , $\approx 3 \text{ km s}^{-1}$ greater than expected for the case of a tidally locked WASP-33 b. We also derive a day-to-night side wind speed of $v_{\text{wind}} = -4.6^{+3.4}_{-3.4} \text{ km s}^{-1}$ where we have included an estimate of the mid-transit time uncertainty in the confidence intervals for v_{wind} .

5.2. Velocity measurements of individual $H\alpha$ transmission spectra

Due to the low signal-to-noise of the individual $H\beta$ transmission spectra, we focus our analysis of the velocity centroids on the $H\alpha$ profiles. Before calculating $v_{H\alpha}$ we shift the spectra in Figure 5 into the rest-frame of the planet. Thus any residual velocity signature is due to mass motion in the planet’s atmosphere or a systematic offset in the calculated in-transit line-of-sight velocities.

Figure 14 shows the in-transit $v_{H\alpha}$ values calculated using Equation 1 and examples of the $H\alpha$ transmission spectra during ingress, in-transit, and egress. The gray shaded region shows where the absorption weakens due to overlap with the local RM profile; we exclude points in this region since the absorption is too weak for a reliable measurement. We note that $v_{H\alpha} = 20.2 \text{ km s}^{-1}$ near $t = 0.4$ hours and is excluded from the plot for clarity.

The uncertainties of the $v_{H\alpha}$ measurements are a combination of two estimates. First, the empirical uncertainties on $v_{H\alpha}$ are of order $\approx 2 - 3 \text{ km s}^{-1}$ which are derived directly from the width and signal-to-noise of the transmission spectra. The second important source of uncertainty is the potential perturbation from a pulse profile. As we demonstrated in Section 4.3 the average perturbation of $v_{H\alpha}$ from a pulse is $\approx 1.7 \text{ km s}^{-1}$. We assume that the pulse uncertainties are independent from the empirical uncertainties and add these quantities in quadrature to obtain the final uncertainties on $v_{H\alpha}$ in Figure 14. We do not include the mid-transit time uncertainty in the $v_{H\alpha}$ uncertainties since this source of error is an offset and would result in the v_{wind} taking on a different value but would not increase the uncertainties on the measurement of $v_{H\alpha}$.

There is striking similarity in the shape of the $v_{H\alpha}$ values when compared with the example rotational models in Figure 2, although there is a noticeable offset towards blue-shifted velocities. The mean value of $v_{H\alpha}$, shown with the horizontal orange line, is similar to the best-fit wind velocity from Section 5.1 ($\overline{v_{H\alpha}} = -1.7 \text{ km s}^{-1}$ versus $v_{\text{wind}} = -4.6 \text{ km s}^{-1}$) where $\overline{v_{H\alpha}}$ is likely skewed towards a smaller blue-shift due to the large positive value of $v_{H\alpha}$ near $t = 0.4$ hours. We note that the shape of the velocity time series cannot be described by spherically expanding atmosphere since the ingress and egress velocities in that case are $\approx 0.0 \text{ km s}^{-1}$. For that

reason we do not consider expansion as an explanatory mechanism for the observations.

5.3. Comparing the velocity centroids to rotational models

In Section 5 we derived a rotational velocity for the atmosphere by applying transmission spectrum models to an average in-transit Balmer line spectrum. As we noted previously, however, there is some degeneracy between broadening mechanisms which may not be fully accounted for with our parameterized models. Another test of the rotational broadening hypothesis is to compare models of varying v_{rot} to the in-transit $v_{H\alpha}$ values with the best-fit value of v_{wind} subtracted off. If rotation is responsible for the shape of the transmission spectra then rotation models should also be able to account for the $v_{H\alpha}$ time series in Figure 14.

To accomplish this we computed a grid of $v_{H\alpha}$ time series models using the framework from Section 5. We generated the models using the best-fit atmospheric parameters from the TRW model in Section 5.1 with the exception of letting v_{rot} vary. We created models for 41 different values of v_{rot} ranging from 0.0 km s^{-1} up to 20.0 km s^{-1} in steps of 0.5 km s^{-1} .

Since the transmission spectra contain the maximal amount of information about atmospheric rotation upon ingress and egress, we only include the first and last four $v_{H\alpha}$ measurements from Figure 14 in the model comparison. The in-transit points are equally consistent with all of the rotational velocities since the line profile centroids at these times are dominated by other effects. Thus the model grid comparison consists of $n = 8$ data points and $m = 1$ free parameter (v_{rot}). Before comparing the data to the model grid we subtract the best-fit value of v_{wind} for the TRW model ($v_{\text{wind}} = -4.6 \text{ km s}^{-1}$) from the measured $v_{H\alpha}$ values Table 3. In principle this leaves only velocities contributions from the rotating atmosphere.

Given the small number of data points and their large individual uncertainties, we opt for a simple χ^2 comparison. For each v_{rot} model we calculate χ^2 between the data and the model interpolated onto the mid-exposure times of the eight selected points. The 68% confidence interval on v_{rot} is then calculated by taking all models for which $\chi^2 < \chi^2_{\text{min}} + \Delta\chi^2$ where $\Delta\chi^2 = 1.0$ in this case (Avni 1976).

We plot the $v_{H\alpha}$ time series with the wind velocity removed in Figure 15, along with the best-fit rotational model (purple line) and the $1 - \sigma$ confidence intervals. We have omitted the velocities measured from the transmission spectra which overlap heavily with the stellar RM profile (gray shaded region). The rotational model

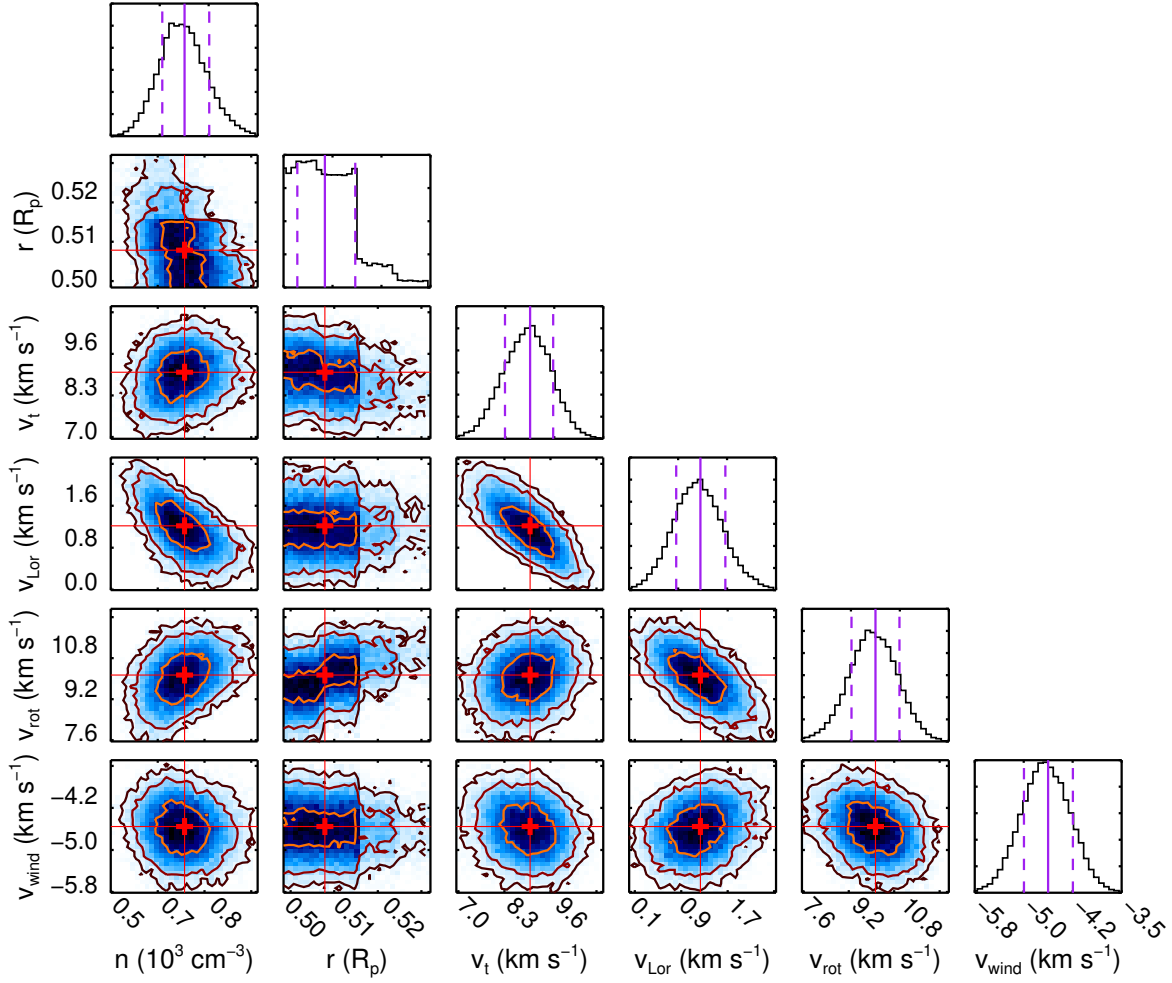


Figure 12. Corner plot of the posteriors for the TRW model. The marginalized parameter histograms are shown at the top of each column and the most-likely parameter value is marked with a vertical purple line; the $1 - \sigma$ confidence intervals are marked with dashed lines. The contours represent the 68%, 95%, and 99% regions of the posteriors.

with $v_{\text{rot}} = 8.5 \text{ km s}^{-1}$ provides the best fit to the data and traces the shape of the $v_{H\alpha}$ measurements during ingress and egress. In addition, the evidence for a rotating atmosphere is strengthened by the fact that the best-fit rotational velocity from the $v_{H\alpha}$ time series is consistent at the $1 - \sigma$ level with the best-fit rotational velocity, $v_{\text{rot}} = 10.1^{+0.8}_{-1.0} \text{ km s}^{-1}$, derived from the transmission spectrum fits.

6. DISCUSSION

We have demonstrated that the velocity centroids of the individual WASP-33 b $H\alpha$ transmission spectra show a pattern consistent with what is expected from a rotating atmosphere. The rotational velocity of $v_{\text{rot}} = 10.1^{+0.8}_{-1.0} \text{ km s}^{-1}$ derived from the average transmission spectrum fit is larger than WASP-33 b's tidally

locked value of $v_{\text{tl}} = 7.1 \text{ km s}^{-1}$. However, the velocity centroid time series analysis results in a smaller rotational velocity of $v_{\text{rot}} = 8.5^{+2.1}_{-1.9}$ which is consistent with the planet's atmosphere rotating at the tidally locked rate. We also find that a large day-to-night side wind velocity of $v_{\text{wind}} = -4.6^{+0.4}_{-0.4} \text{ km s}^{-1}$ is required to explain the blue-shifted transmission spectra. The wind velocity becomes less significant, $v_{\text{wind}} = -4.6^{+3.4}_{-3.4} \text{ km s}^{-1}$, when we consider uncertainties in the mid-transit time and how this affects the global velocity offset of the transmission spectra.

Measuring a planet's rotational velocity via its transmission spectrum is dependent on the assumption that the rotational axis is perpendicular to the orbital plane. Thus we are in fact constraining the value $v_{\text{rot}} \sin i$ where i is the angle between the rotation axis and the planet's

Table 3. Balmer line model fit parameters

| | n | r | v_t | v_{Lor} | v_{rot} | v_{wind}^\dagger | v_{jet} | |
|---------------------|----------------------|------------------------|------------------------|------------------------|------------------------|---------------------------|------------------------|--------------------|
| Model | (cm^{-3}) | (R_p) | (km s^{-1}) | (km s^{-1}) | (km s^{-1}) | (km s^{-1}) | (km s^{-1}) | ΔBIC |
| (1) | (2) | (3) | (4) | (5) | (6) | (7) | (8) | (9) |
| T* | 433^{+139}_{-96} | $0.48^{+0.04}_{-0.04}$ | $3.8^{+1.1}_{-1.6}$ | $5.2^{+0.5}_{-0.7}$ | ... | ... | ... | ... |
| TW | 541^{+168}_{-87} | $0.50^{+0.04}_{-0.04}$ | $7.8^{+0.9}_{-1.1}$ | $3.6^{+0.7}_{-0.6}$ | ... | $-3.5^{+0.5}_{-0.5}$ | ... | -440 |
| TR | 463^{+117}_{-95} | $0.49^{+0.04}_{-0.04}$ | $4.3^{+1.1}_{-1.1}$ | $5.0^{+0.6}_{-0.7}$ | $1.8^{+3.1}_{-1.5}$ | ... | ... | -9 |
| TRW | 808^{+94}_{-93} | $0.51^{+0.04}_{-0.04}$ | $8.9^{+0.7}_{-0.7}$ | $1.3^{+0.5}_{-0.4}$ | $10.1^{+0.8}_{-1.0}$ | $-4.6^{+0.4}_{-0.4}$ | ... | -477 |
| TJ | 554^{+150}_{-123} | $0.50^{+0.04}_{-0.04}$ | $4.3^{+1.1}_{-1.3}$ | $3.7^{+0.6}_{-0.6}$ | ... | ... | $20.4^{+8.0}_{-7.6}$ | -5 |
| TWJ | 666^{+85}_{-77} | $0.51^{+0.04}_{-0.04}$ | $7.3^{+0.9}_{-0.8}$ | $2.4^{+0.4}_{-0.4}$ | ... | $-3.6^{+0.4}_{-0.4}$ | $19.2^{+2.3}_{-2.6}$ | -458 |
| TRWJ | 826^{+100}_{-99} | $0.52^{+0.04}_{-0.04}$ | $8.7^{+0.8}_{-0.9}$ | $0.9^{+0.5}_{-0.5}$ | $7.2^{+1.2}_{-0.9}$ | $-4.7^{+0.5}_{-0.4}$ | $19.1^{+3.1}_{-9.3}$ | -477 |
| TWJ+R _{t1} | 777^{+100}_{-92} | $0.55^{+0.04}_{-0.04}$ | $8.0^{+0.8}_{-0.8}$ | $0.9^{+0.4}_{-0.3}$ | 7.1 | $-4.7^{+0.4}_{-0.4}$ | $20.1^{+2.8}_{-2.4}$ | -486 |

[†] Table values only include uncertainties from the model fitting and do not take into account the uncertainty in T_0 (see [subsubsection 5.1.1](#))

* Abbreviations: T = Thermal, R = Rotation, W = Wind, J = Jet

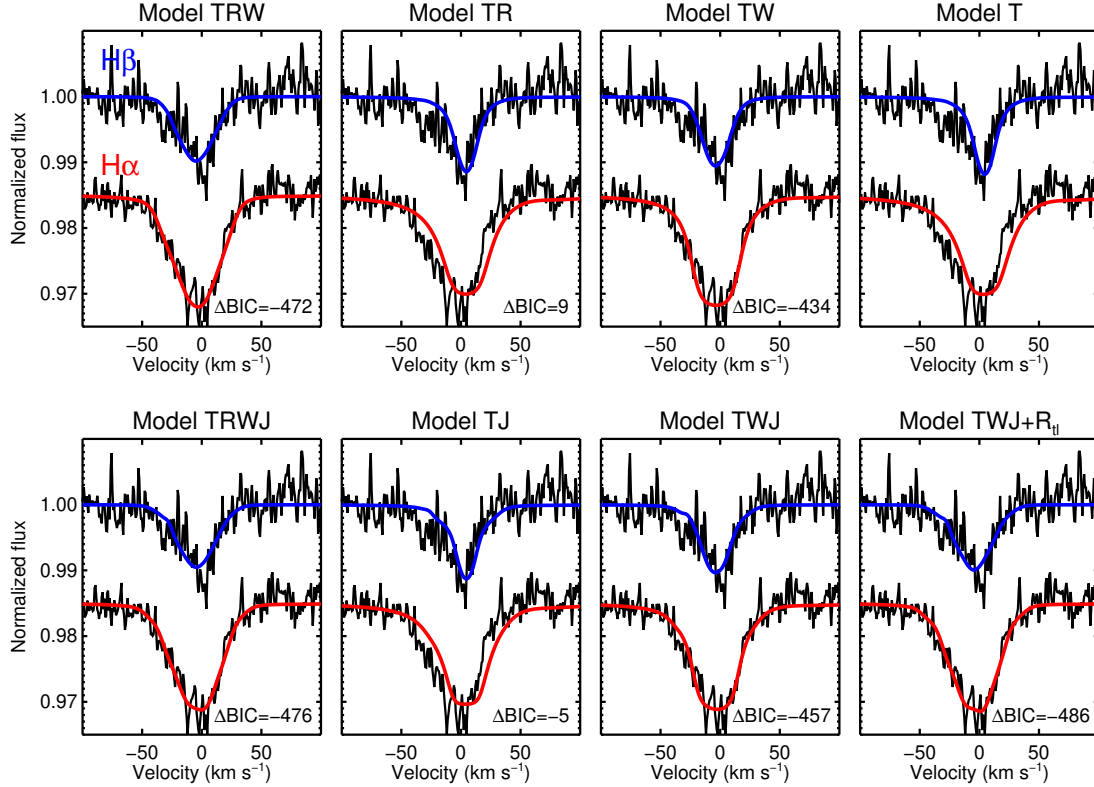


Figure 13. Atmospheric model fits (solid colored lines) to the Balmer line transmission spectra (black). The difference between the BIC of each model and that of the Thermal model (top right panel, Model T) is given in the lower-right of each plot window. The model which includes a day-to-night side wind, rotation, and thermal broadening (Model TRW) is strongly preferred over the other models. Although including an equatorial jet results in an equally good or better description of the data (Models TRWJ and TWJ+R_{t1}) the jet velocities are non-physical.

orbital plane. The angle between the planet's rotation axis and its transit chord, restricted to the plane of the

sky, will also affect the measured velocity centroids: if this angle is 0° then the ingress and egress velocity cen-

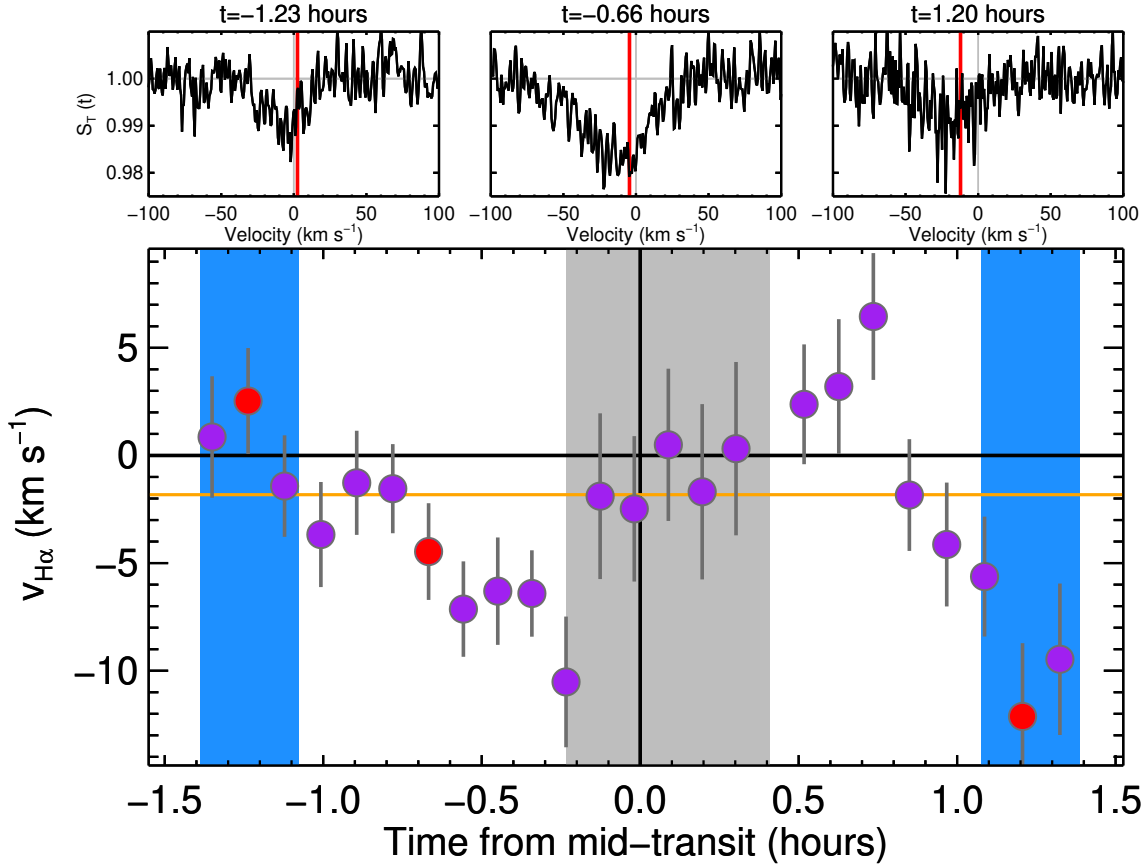


Figure 14. Measured $v_{H\alpha}$ values for the in-transit $H\alpha$ transmission spectra. The blue shaded regions show ingress and egress times and the gray shaded mark the portion of the transit for which there is little or no absorption due to the planet’s velocity overlapping with the local stellar RM signal. Example transmission spectra are shown above the velocity plot where the red plot symbols correspond to the $v_{H\alpha}$ values of the example spectra. The orange line marks the mean of the $v_{H\alpha}$ values. The best-fit wind velocity from Section 5.1 is similar to the mean $v_{H\alpha}$ value and the structure of the velocities is comparable to the rotational velocity examples in Figure 2.

troids will be $\approx 0 \text{ km s}^{-1}$ since the velocities at the poles are symmetric around the planet’s rotation axis. If the angle is 90° then the centroid velocities will be maximized during ingress and egress. This analysis provides another possible avenue for constraining the orbit geometry: if the rotational broadening from the average transmission spectrum is consistent with the time-series rotational velocity then the angle between the rotation axis and the transit chord must be $\approx 90^\circ$. The agreement between the rotational velocities from our average spectrum model and the time-series grid model supports the conclusion that WASP-33 b’s rotation axis is perpendicular, or only slightly inclined, to its orbital plane and also to its transit chord across the star.

A second notable result from our analysis is the large blue-shift seen in the transmission spectrum. Our model finds that a day-to-night side wind of $v_{\text{wind}} = -4.6^{+3.4}_{-3.4} \text{ km s}^{-1}$ can account for this shift. A large in-transit blue-shift of $-11 \pm 0.7 \text{ km s}^{-1}$ was recently measured for the

UHJ WASP-76 b in the cross-correlation function of the planet’s neutral iron absorption lines (Ehrenreich et al. 2020). While the uncertainties in our measured mid-transit timing prevent us from establishing the absolute blue-shift of the transmission spectrum with more precision, wind velocities of $\approx 5 \text{ km s}^{-1}$ are not commonly seen for hot and ultra-hot planets. For example, Yan & Henning (2018), Cauley et al. (2019a), and Wyttenbach et al. (2020) all found no evidence of a velocity shift in the transmission spectrum of KELT-9 b, currently the hottest transiting gas giant to be studied in detail. Most measured transmission spectrum velocities in hot planet atmospheres are on the order of $\approx 2 \text{ km s}^{-1}$ (e.g., Wyttenbach et al. 2015; Casasayas-Barris et al. 2017). Our results, combined with those from Ehrenreich et al. (2020), hint that the average day-to-night side wind speed increases into the ultra-hot atmosphere regime ($T_{\text{eq}} > 2000$; Parmentier et al. 2018; Baxter et al. 2020) but these flows are disrupted in the extreme lim-

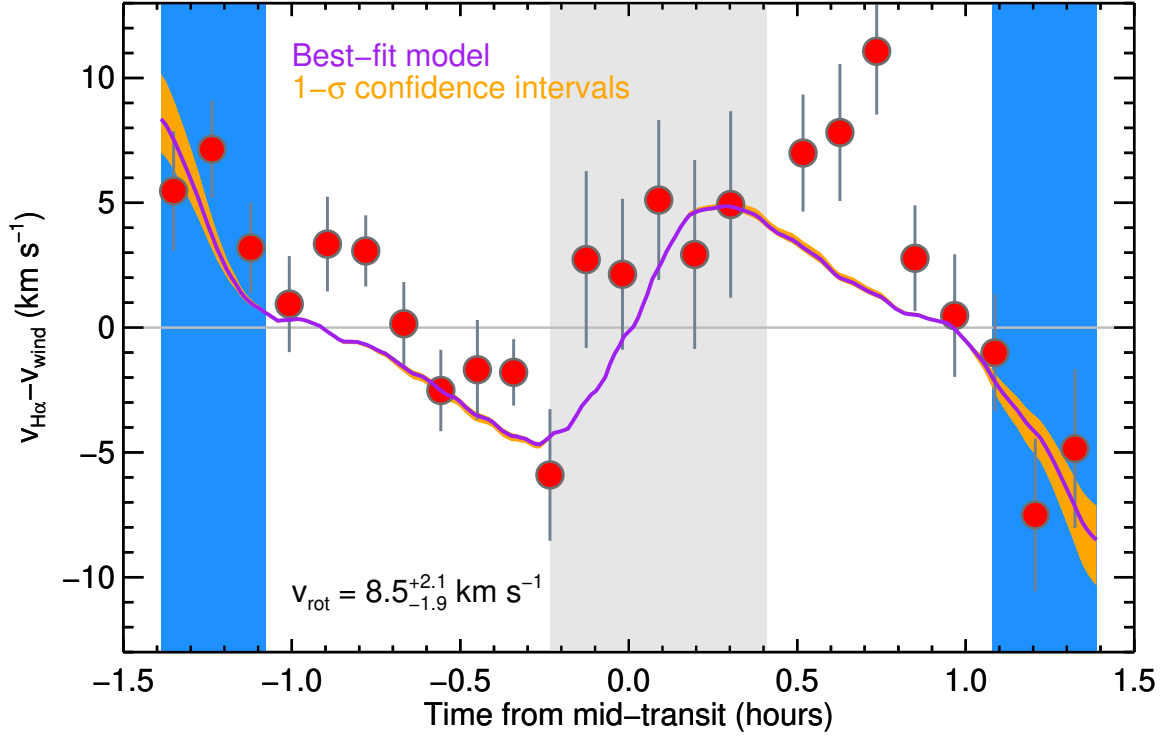


Figure 15. Same as Figure 14 but now with the best-fit day-to-night side wind velocity v_{wind} from Table 3 removed. The rotational model with the minimum χ^2 value is shown in purple and the estimated $1 - \sigma$ confidence intervals are shaded orange. Only the first and last four velocities are included in the model comparison. The best-fit rotational velocity of 8.5 km s^{-1} is consistent with that found from the average transmission spectrum fits.

its of an atmosphere like KELT-9 b’s at $T_{\text{eq}} = 4000 \text{ K}$. Indeed, Komacek & Showman (2020) showed that wind speeds on the order of $\approx 5 - 6 \text{ km s}^{-1}$ are possible at pressures of 1 mbar for UHJ atmospheres.

In their analysis of Ca II H and K and infrared triplet absorption in WASP-33 b’s atmosphere Yan et al. (2019) do not see a consistent blue-shift in the two sets of lines. A blue-shift similar in magnitude to what we measure would likely have been detected in their investigation. The same caveats with regards to the mid-transit time uncertainty apply to their procedure so it is possible that the true blue-shift is simply masked by inherent uncertainties in the adopted mid-transit time. The Balmer lines and the Ca II lines are expected to form at similar pressures in UHJ atmospheres so we do not expect the velocity flows sampled by the lines to differ significantly (Turner et al. 2020). Given the discrepancies between our velocity measurement and those from Yan et al. (2019) we suggest that a concrete interpretation of the day-to-night side wind signature await additional spectroscopic transit studies. High-quality simultaneous photometry would aid in reducing the mid-transit time uncertainty for the spectroscopic analysis.

Although our models are able to account for the morphology and velocity centroids of WASP-33 b’s Balmer line transmission spectra, a more realistic treatment of velocity flows in the planet’s thermosphere could reveal important information about which velocity features contribute to the line profiles (e.g., Flowers et al. 2019). For example, the atmosphere is likely not rigidly rotating from the stratosphere out to the edge of the thermosphere and jets, which are a ubiquitous feature of hot planet GCMs (e.g., Rauscher & Menou 2010; Showman et al. 2013; Carone et al. 2020; Komacek & Showman 2020), probably contribute to the transmission spectrum even though they are not discernible in our model treatment of the line profiles.

Finally, we emphasize the need for GCM exploration of the uppermost bound atmospheric layers of hot and ultra-hot planets. Such simulations are currently difficult to achieve primarily due to the breakdown of the primitive equations of meteorology at micro- and nanobar pressures. Atomic absorption lines in hot planet atmospheres generally trace these low-pressure layers and they are relatively straightforward to measure. Thus the rapidly growing number of hot planet atmosphere detections, and their associated velocity signatures, needs a

better theoretical platform upon which to interpret any observed velocity signatures rather than extrapolating from the abundance of GCM results at higher pressures.

7. CONCLUSIONS

We have presented the first detections of the Balmer lines $H\alpha$ and $H\beta$ in the atmosphere of WASP-33 b and measured the velocity centroids of the individual $H\alpha$ transmission spectra as a function of time throughout the transit. Both the velocity centroids ($v_{\text{rot}} = 8.5^{+2.1}_{-1.9}$ km s⁻¹) and the rotational broadening measured from the in-transit spectrum ($v_{\text{rot}} = 10.1^{+0.8}_{-1.0}$ km s⁻¹) are consistent with a super-rotating atmosphere, although the time-series $H\alpha$ velocities are also in agreement with the expected tidally-locked rotation rate of WASP-33 b at the $1 - \sigma$ level. We do not find any evidence of velocity signatures associated with equatorial jets, although such features may be swamped by the planet’s fast rotation and possibly not retrievable using the Balmer line transmission spectra.

Our observations demonstrate the power of time-resolved transmission spectra where the signal-to-noise of individual exposures permit reliable extraction of the profile morphologies and velocity centroids. Time-series measurements of velocity features in hot planet atmospheres can help resolve the line broadening degeneracy

between, for example, spherical expansion and rotation due to the very different velocity time-series produced by each feature. The advent of 30-meter telescopes will greatly expand the parameter space for which these experiments are possible and may enable variability studies (e.g., Komacek & Showman 2020) of velocity flows in the atmospheres of transiting exoplanets. Empirical constraints on atmospheric velocity dynamics are a critical part of our ongoing pursuit of a more complete understanding of the physics of exoplanets.

This research has made use of the NASA Exoplanet Archive, which is operated by the California Institute of Technology, under contract with the National Aeronautics and Space Administration under the Exoplanet Exploration Program. Additionally, this work has made use of NASA’s Astrophysical Data System and of the SIMBAD database, which is operated at CDS, Strasbourg, France. This work has also made use of the VALD database, operated at Uppsala University, the Institute of Astronomy RAS in Moscow, and the University of Vienna. We thank the staff at the Large Binocular Telescope for their role in collecting the data presented in this manuscript.

Software: EXOFAST, Eastman et al. (2013); Molecfit, Kausch et al. (2015); Spectroscopy Made Easy (SME), Valenti & Piskunov (1996); Piskunov & Valenti (2017)

REFERENCES

- Allart, R., Bourrier, V., Lovis, C., et al. 2018, *Science*, 362, 1384, doi: [10.1126/science.aat5879](https://doi.org/10.1126/science.aat5879)
- . 2019, *A&A*, 623, A58, doi: [10.1051/0004-6361/201834917](https://doi.org/10.1051/0004-6361/201834917)
- Allers, K. N., Vos, J. M., Biller, B. A., & Williams, P. K. G. 2020, *Science*, 368, 169, doi: [10.1126/science.aaz2856](https://doi.org/10.1126/science.aaz2856)
- Apai, D., Karalidi, T., Marley, M. S., et al. 2017, *Science*, 357, 683, doi: [10.1126/science.aam9848](https://doi.org/10.1126/science.aam9848)
- Avni, Y. 1976, *ApJ*, 210, 642, doi: [10.1086/154870](https://doi.org/10.1086/154870)
- Baraffe, I., Chabrier, G., Barman, T. S., Allard, F., & Hauschildt, P. H. 2003, *A&A*, 402, 701, doi: [10.1051/0004-6361:20030252](https://doi.org/10.1051/0004-6361:20030252)
- Barstow, J. K., Aigrain, S., Irwin, P. G. J., & Sing, D. K. 2017, *ApJ*, 834, 50, doi: [10.3847/1538-4357/834/1/50](https://doi.org/10.3847/1538-4357/834/1/50)
- Baxter, C., Désert, J.-M., Parmentier, V., et al. 2020, *A&A*, 639, A36, doi: [10.1051/0004-6361/201937394](https://doi.org/10.1051/0004-6361/201937394)
- Beatty, T. G., Marley, M. S., Gaudi, B. S., et al. 2019, *AJ*, 158, 166, doi: [10.3847/1538-3881/ab33fc](https://doi.org/10.3847/1538-3881/ab33fc)
- Ben-Yami, M., Madhusudhan, N., Cabot, S. H. C., et al. 2020, *ApJL*, 897, L5, doi: [10.3847/2041-8213/ab94aa](https://doi.org/10.3847/2041-8213/ab94aa)
- Bourrier, V., Lecavelier des Etangs, A., Dupuy, H., et al. 2013, *A&A*, 551, A63, doi: [10.1051/0004-6361/201220533](https://doi.org/10.1051/0004-6361/201220533)
- Bourrier, V., Lecavelier des Etangs, A., Ehrenreich, D., et al. 2018, *A&A*, 620, A147, doi: [10.1051/0004-6361/201833675](https://doi.org/10.1051/0004-6361/201833675)
- Bourrier, V., Ehrenreich, D., Lendl, M., et al. 2020, *A&A*, 635, A205, doi: [10.1051/0004-6361/201936640](https://doi.org/10.1051/0004-6361/201936640)
- Brogi, M., de Kok, R. J., Albrecht, S., et al. 2016, *ApJ*, 817, 106, doi: [10.3847/0004-637X/817/2/106](https://doi.org/10.3847/0004-637X/817/2/106)
- Brogi, M., & Line, M. R. 2019, *AJ*, 157, 114, doi: [10.3847/1538-3881/aaffd3](https://doi.org/10.3847/1538-3881/aaffd3)
- Carone, L., Baeyens, R., Mollière, P., et al. 2020, *MNRAS*, 496, 3582, doi: [10.1093/mnras/staa1733](https://doi.org/10.1093/mnras/staa1733)
- Casasayas-Barris, N., Palle, E., Nowak, G., et al. 2017, *A&A*, 608, A135, doi: [10.1051/0004-6361/201731956](https://doi.org/10.1051/0004-6361/201731956)
- Casasayas-Barris, N., Pallé, E., Yan, F., et al. 2019, *A&A*, 628, A9, doi: [10.1051/0004-6361/201935623](https://doi.org/10.1051/0004-6361/201935623)
- Cauley, P. W., Kuckein, C., Redfield, S., et al. 2018, *AJ*, 156, 189, doi: [10.3847/1538-3881/aaddf9](https://doi.org/10.3847/1538-3881/aaddf9)
- Cauley, P. W., Redfield, S., & Jensen, A. G. 2017, *AJ*, 153, 217, doi: [10.3847/1538-3881/aa6a15](https://doi.org/10.3847/1538-3881/aa6a15)

- Cauley, P. W., Shkolnik, E. L., Ilyin, I., et al. 2019a, *AJ*, 157, 69, doi: [10.3847/1538-3881/aaf725](https://doi.org/10.3847/1538-3881/aaf725)
- Cauley, P. W., Shkolnik, E. L., Llama, J., & Lanza, A. F. 2019b, *Nature Astronomy*, 408, doi: [10.1038/s41550-019-0840-x](https://doi.org/10.1038/s41550-019-0840-x)
- Chakrabarty, A., & Sengupta, S. 2019, *AJ*, 158, 39, doi: [10.3847/1538-3881/ab24dd](https://doi.org/10.3847/1538-3881/ab24dd)
- Collier Cameron, A., Guenther, E., Smalley, B., et al. 2010, *MNRAS*, 407, 507, doi: [10.1111/j.1365-2966.2010.16922.x](https://doi.org/10.1111/j.1365-2966.2010.16922.x)
- Czesla, S., Klocová, T., Khalafinejad, S., Wolter, U., & Schmitt, J. H. M. M. 2015, *A&A*, 582, A51, doi: [10.1051/0004-6361/201526386](https://doi.org/10.1051/0004-6361/201526386)
- Eastman, J., Gaudi, B. S., & Agol, E. 2013, *PASP*, 125, 83, doi: [10.1086/669497](https://doi.org/10.1086/669497)
- Ehrenreich, D., Bourrier, V., Wheatley, P. J., et al. 2015, *Nature*, 522, 459, doi: [10.1038/nature14501](https://doi.org/10.1038/nature14501)
- Ehrenreich, D., Lovis, C., Allart, R., et al. 2020, *Nature*, 580, 597, doi: [10.1038/s41586-020-2107-1](https://doi.org/10.1038/s41586-020-2107-1)
- Evans, T. M., Sing, D. K., Kataria, T., et al. 2017, *Nature*, 548, 58, doi: [10.1038/nature23266](https://doi.org/10.1038/nature23266)
- Flowers, E., Brogi, M., Rauscher, E., Kempton, E. M. R., & Chiavassa, A. 2019, *AJ*, 157, 209, doi: [10.3847/1538-3881/ab164c](https://doi.org/10.3847/1538-3881/ab164c)
- Foreman-Mackey, D., Hogg, D. W., Lang, D., & Goodman, J. 2013, *PASP*, 125, 306, doi: [10.1086/670067](https://doi.org/10.1086/670067)
- Gao, P., Thorngren, D. P., Lee, G. K. H., et al. 2020, *Nature Astronomy*, doi: [10.1038/s41550-020-1114-3](https://doi.org/10.1038/s41550-020-1114-3)
- García Muñoz, A., & Schneider, P. C. 2019, *ApJL*, 884, L43, doi: [10.3847/2041-8213/ab498d](https://doi.org/10.3847/2041-8213/ab498d)
- Gibson, N. P., Merritt, S., Nugroho, S. K., et al. 2020, *MNRAS*, 493, 2215, doi: [10.1093/mnras/staa228](https://doi.org/10.1093/mnras/staa228)
- Goodman, J., & Weare, J. 2010, *Communications in Applied Mathematics and Computational Science*, 5, 65, doi: [10.2140/camcos.2010.5.65](https://doi.org/10.2140/camcos.2010.5.65)
- Herrero, E., Morales, J. C., Ribas, I., & Naves, R. 2011, *A&A*, 526, L10, doi: [10.1051/0004-6361/201015875](https://doi.org/10.1051/0004-6361/201015875)
- Hirano, T., Suto, Y., Winn, J. N., et al. 2011, *ApJ*, 742, 69, doi: [10.1088/0004-637X/742/2/69](https://doi.org/10.1088/0004-637X/742/2/69)
- Hoeijmakers, H. J., Ehrenreich, D., Heng, K., et al. 2018, *Nature*, 560, 453, doi: [10.1038/s41586-018-0401-y](https://doi.org/10.1038/s41586-018-0401-y)
- Hoeijmakers, H. J., Ehrenreich, D., Kitzmann, D., et al. 2019, *A&A*, 627, A165, doi: [10.1051/0004-6361/201935089](https://doi.org/10.1051/0004-6361/201935089)
- Huang, C., Arras, P., Christie, D., & Li, Z.-Y. 2017, *ApJ*, 851, 150, doi: [10.3847/1538-4357/aa9b32](https://doi.org/10.3847/1538-4357/aa9b32)
- Iorio, L. 2011, *Ap&SS*, 331, 485, doi: [10.1007/s10509-010-0468-x](https://doi.org/10.1007/s10509-010-0468-x)
- Jensen, A. G., Cauley, P. W., Redfield, S., Cochran, W. D., & Endl, M. 2018, *AJ*, 156, 154, doi: [10.3847/1538-3881/aadca7](https://doi.org/10.3847/1538-3881/aadca7)
- Johnson, M. C., Cochran, W. D., Collier Cameron, A., & Bayliss, D. 2015, *ApJL*, 810, L23, doi: [10.1088/2041-8205/810/2/L23](https://doi.org/10.1088/2041-8205/810/2/L23)
- Kataria, T., Showman, A. P., Fortney, J. J., et al. 2015, *ApJ*, 801, 86, doi: [10.1088/0004-637X/801/2/86](https://doi.org/10.1088/0004-637X/801/2/86)
- Kausch, W., Noll, S., Smette, A., et al. 2015, *A&A*, 576, A78, doi: [10.1051/0004-6361/201423909](https://doi.org/10.1051/0004-6361/201423909)
- Keles, E., Mallonn, M., von Essen, C., et al. 2019, *MNRAS*, L124, doi: [10.1093/mnras/slz123](https://doi.org/10.1093/mnras/slz123)
- Knutson, H. A., Lewis, N., Fortney, J. J., et al. 2012, *ApJ*, 754, 22, doi: [10.1088/0004-637X/754/1/22](https://doi.org/10.1088/0004-637X/754/1/22)
- Komacek, T. D., & Showman, A. P. 2020, *ApJ*, 888, 2, doi: [10.3847/1538-4357/ab5b0b](https://doi.org/10.3847/1538-4357/ab5b0b)
- Kreidberg, L., Bean, J. L., Désert, J.-M., et al. 2014, *Nature*, 505, 69, doi: [10.1038/nature12888](https://doi.org/10.1038/nature12888)
- Lavie, B., Ehrenreich, D., Bourrier, V., et al. 2017, *A&A*, 605, L7, doi: [10.1051/0004-6361/201713140](https://doi.org/10.1051/0004-6361/201713140)
- Lehmann, H., Guenther, E., Sebastian, D., et al. 2015, *A&A*, 578, L4, doi: [10.1051/0004-6361/201526176](https://doi.org/10.1051/0004-6361/201526176)
- Libby-Roberts, J. E., Berta-Thompson, Z. K., Désert, J.-M., et al. 2020, *AJ*, 159, 57, doi: [10.3847/1538-3881/ab5d36](https://doi.org/10.3847/1538-3881/ab5d36)
- Line, M. R., Knutson, H., Wolf, A. S., & Yung, Y. L. 2014, *ApJ*, 783, 70, doi: [10.1088/0004-637X/783/2/70](https://doi.org/10.1088/0004-637X/783/2/70)
- Line, M. R., Stevenson, K. B., Bean, J., et al. 2016, *AJ*, 152, 203, doi: [10.3847/0004-6256/152/6/203](https://doi.org/10.3847/0004-6256/152/6/203)
- Louden, T., & Wheatley, P. J. 2015, *ApJ*, 814, L24, doi: [10.1088/2041-8205/814/2/L24](https://doi.org/10.1088/2041-8205/814/2/L24)
- Miller-Ricci Kempton, E., & Rauscher, E. 2012, *ApJ*, 751, 117, doi: [10.1088/0004-637X/751/2/117](https://doi.org/10.1088/0004-637X/751/2/117)
- Moran, S. E., Hörst, S. M., Batalha, N. E., Lewis, N. K., & Wakeford, H. R. 2018, *AJ*, 156, 252, doi: [10.3847/1538-3881/aae83a](https://doi.org/10.3847/1538-3881/aae83a)
- Nikolov, N., Sing, D. K., Goyal, J., et al. 2018, *MNRAS*, 474, 1705, doi: [10.1093/mnras/stx2865](https://doi.org/10.1093/mnras/stx2865)
- Nugroho, S. K., Gibson, N. P., de Mooij, E. J. W., et al. 2020a, *ApJL*, 898, L31, doi: [10.3847/2041-8213/aba4b6](https://doi.org/10.3847/2041-8213/aba4b6)
- . 2020b, *MNRAS*, 496, 504, doi: [10.1093/mnras/staa1459](https://doi.org/10.1093/mnras/staa1459)
- Nugroho, S. K., Kawahara, H., Masuda, K., et al. 2017, *AJ*, 154, 221, doi: [10.3847/1538-3881/aa9433](https://doi.org/10.3847/1538-3881/aa9433)
- Parmentier, V., Line, M. R., Bean, J. L., et al. 2018, *A&A*, 617, A110, doi: [10.1051/0004-6361/201833059](https://doi.org/10.1051/0004-6361/201833059)
- Pino, L., Désert, J.-M., Brogi, M., et al. 2020, *ApJL*, 894, L27, doi: [10.3847/2041-8213/ab8c44](https://doi.org/10.3847/2041-8213/ab8c44)
- Piskunov, N., & Valenti, J. A. 2017, *A&A*, 597, A16, doi: [10.1051/0004-6361/201629124](https://doi.org/10.1051/0004-6361/201629124)
- Rauscher, E., & Menou, K. 2010, *ApJ*, 714, 1334, doi: [10.1088/0004-637X/714/2/1334](https://doi.org/10.1088/0004-637X/714/2/1334)
- . 2013, *ApJ*, 764, 103, doi: [10.1088/0004-637X/764/1/103](https://doi.org/10.1088/0004-637X/764/1/103)

- Ridden-Harper, A. R., Snellen, I. A. G., Keller, C. U., et al. 2016, *A&A*, 593, A129, doi: [10.1051/0004-6361/201628448](https://doi.org/10.1051/0004-6361/201628448)
- Rogers, T. M. 2017, *Nature Astronomy*, 1, 0131, doi: [10.1038/s41550-017-0131](https://doi.org/10.1038/s41550-017-0131)
- Salz, M., Czesla, S., Schneider, P. C., & Schmitt, J. H. M. M. 2016, *A&A*, 586, A75, doi: [10.1051/0004-6361/201526109](https://doi.org/10.1051/0004-6361/201526109)
- Salz, M., Czesla, S., Schneider, P. C., et al. 2018, *A&A*, 620, A97, doi: [10.1051/0004-6361/201833694](https://doi.org/10.1051/0004-6361/201833694)
- Seidel, J. V., Ehrenreich, D., Pino, L., et al. 2019, arXiv e-prints, arXiv:1912.02787. <https://arxiv.org/abs/1912.02787>
- Showman, A. P., Fortney, J. J., Lewis, N. K., & Shabram, M. 2013, *ApJ*, 762, 24, doi: [10.1088/0004-637X/762/1/24](https://doi.org/10.1088/0004-637X/762/1/24)
- Showman, A. P., & Guillot, T. 2002, *A&A*, 385, 166, doi: [10.1051/0004-6361:20020101](https://doi.org/10.1051/0004-6361:20020101)
- Showman, A. P., & Polvani, L. M. 2011, *ApJ*, 738, 71, doi: [10.1088/0004-637X/738/1/71](https://doi.org/10.1088/0004-637X/738/1/71)
- Sing, D. K., Lavvas, P., Ballester, G. E., et al. 2019, *AJ*, 158, 91, doi: [10.3847/1538-3881/ab2986](https://doi.org/10.3847/1538-3881/ab2986)
- Snellen, I. A. G., Brandl, B. R., de Kok, R. J., et al. 2014, *Nature*, 509, 63, doi: [10.1038/nature13253](https://doi.org/10.1038/nature13253)
- Snellen, I. A. G., de Kok, R. J., de Mooij, E. J. W., & Albrecht, S. 2010, *Nature*, 465, 1049, doi: [10.1038/nature09111](https://doi.org/10.1038/nature09111)
- Spake, J. J., Sing, D. K., Evans, T. M., et al. 2018, *Nature*, 557, 68, doi: [10.1038/s41586-018-0067-5](https://doi.org/10.1038/s41586-018-0067-5)
- Spiegel, D. S., & Burrows, A. 2013, *ApJ*, 772, 76, doi: [10.1088/0004-637X/772/1/76](https://doi.org/10.1088/0004-637X/772/1/76)
- Stangret, M., Casasayas-Barris, N., Pallé, E., et al. 2020, *A&A*, 638, A26, doi: [10.1051/0004-6361/202037541](https://doi.org/10.1051/0004-6361/202037541)
- Strassmeier, K. G., Ilyin, I., & Steffen, M. 2018, *A&A*, 612, A44, doi: [10.1051/0004-6361/201731631](https://doi.org/10.1051/0004-6361/201731631)
- Strassmeier, K. G., Ilyin, I., Järvinen, A., et al. 2015, *Astronomische Nachrichten*, 336, 324, doi: [10.1002/asna.201512172](https://doi.org/10.1002/asna.201512172)
- Turner, J. D., Pearson, K. A., Biddle, L. I., et al. 2016, *MNRAS*, 459, 789, doi: [10.1093/mnras/stw574](https://doi.org/10.1093/mnras/stw574)
- Turner, J. D., de Mooij, E. J. W., Jayawardhana, R., et al. 2020, *ApJL*, 888, L13, doi: [10.3847/2041-8213/ab60a9](https://doi.org/10.3847/2041-8213/ab60a9)
- Valenti, J. A., & Piskunov, N. 1996, *A&AS*, 118, 595
- von Essen, C., Mallonn, M., Borre, C. C., et al. 2020, *A&A*, 639, A34, doi: [10.1051/0004-6361/202037905](https://doi.org/10.1051/0004-6361/202037905)
- von Essen, C., Mallonn, M., Welbanks, L., et al. 2019, *A&A*, 622, A71, doi: [10.1051/0004-6361/201833837](https://doi.org/10.1051/0004-6361/201833837)
- von Essen, C., Czesla, S., Wolter, U., et al. 2014, *A&A*, 561, A48, doi: [10.1051/0004-6361/201322453](https://doi.org/10.1051/0004-6361/201322453)
- Wang, J., David, T. J., Hillenbrand, L. A., et al. 2018, *ApJ*, 865, 141, doi: [10.3847/1538-4357/aadee8](https://doi.org/10.3847/1538-4357/aadee8)
- Watanabe, N., Narita, N., & Johnson, M. C. 2020, *PASJ*, 72, 19, doi: [10.1093/pasj/psz140](https://doi.org/10.1093/pasj/psz140)
- Wong, I., Knutson, H. A., Kataria, T., et al. 2016, *ApJ*, 823, 122, doi: [10.3847/0004-637X/823/2/122](https://doi.org/10.3847/0004-637X/823/2/122)
- Wong, I., Shporer, A., Kitzmann, D., et al. 2020, *AJ*, 160, 88, doi: [10.3847/1538-3881/aba2cb](https://doi.org/10.3847/1538-3881/aba2cb)
- Wytttenbach, A., Ehrenreich, D., Lovis, C., Udry, S., & Pepe, F. 2015, *A&A*, 577, A62, doi: [10.1051/0004-6361/201525729](https://doi.org/10.1051/0004-6361/201525729)
- Wytttenbach, A., Mollière, P., Ehrenreich, D., et al. 2020, *A&A*, 638, A87, doi: [10.1051/0004-6361/201937316](https://doi.org/10.1051/0004-6361/201937316)
- Yan, F., & Henning, T. 2018, *Nature Astronomy*, 2, 714, doi: [10.1038/s41550-018-0503-3](https://doi.org/10.1038/s41550-018-0503-3)
- Yan, F., Pallé, E., Fosbury, R. A. E., Petr-Gotzens, M. G., & Henning, T. 2017, *A&A*, 603, A73, doi: [10.1051/0004-6361/201630144](https://doi.org/10.1051/0004-6361/201630144)
- Yan, F., Casasayas-Barris, N., Molaverdikhani, K., et al. 2019, *A&A*, 632, A69, doi: [10.1051/0004-6361/201936396](https://doi.org/10.1051/0004-6361/201936396)
- Yan, F., Pallé, E., Reiners, A., et al. 2020, *A&A*, 640, L5, doi: [10.1051/0004-6361/202038294](https://doi.org/10.1051/0004-6361/202038294)

APPENDIX

A. INDIVIDUAL TRANSMISSION SPECTRA PLOTS

In this appendix we provide the individual in-transit transmission spectra for $H\alpha$ and $H\beta$ in the rest frame of the planet. All $H\alpha$ spectra have been binned by a factor of 2 and the $H\beta$ spectra were binned by a factor of 5 for clarity.

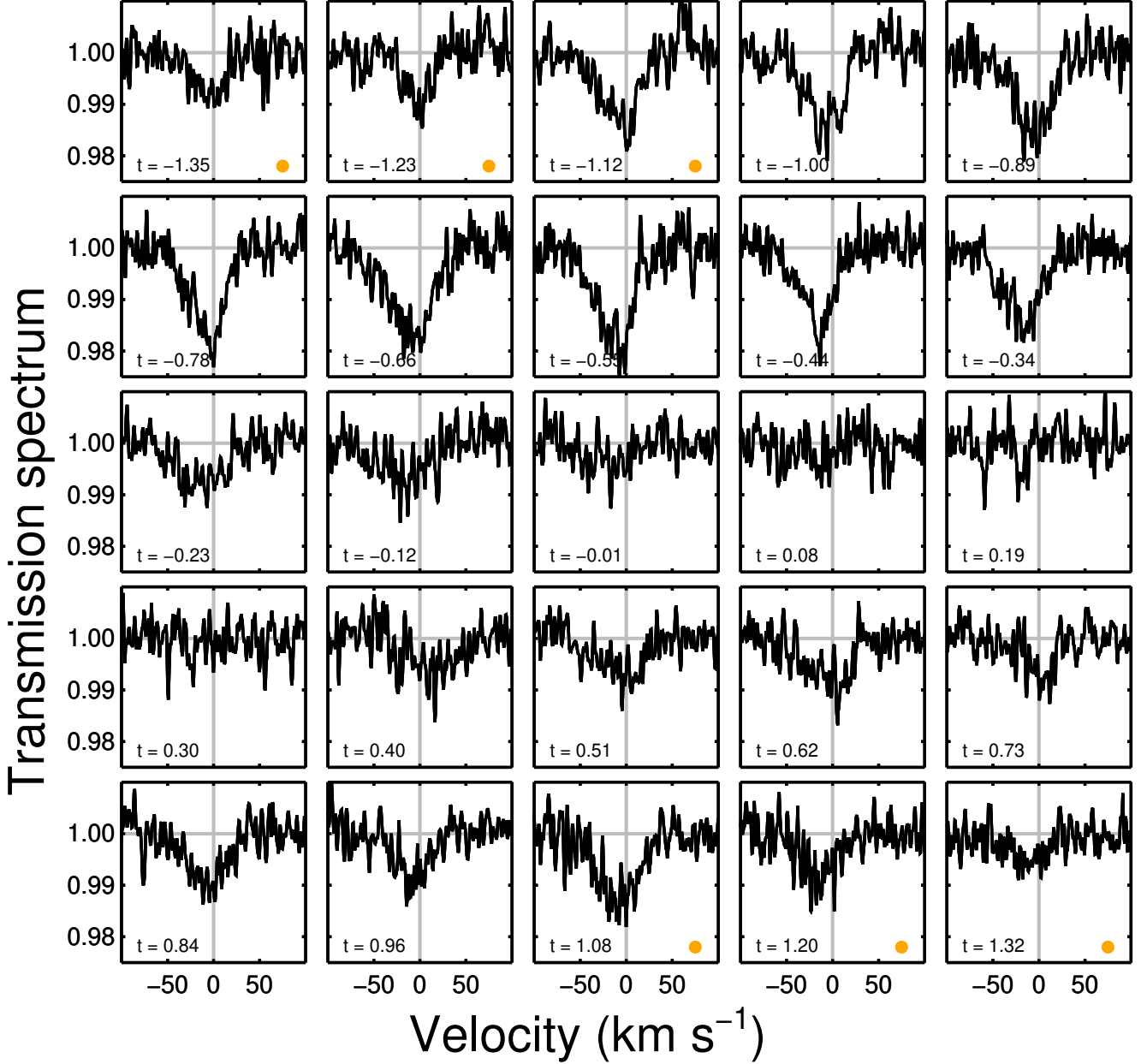


Figure 16. In-transit $H\alpha$ transmission spectra in the planetary rest frame. Mid-exposure times are marked in hours in the bottom left of each panel. The vertical gray line marks $v = 0.0 \text{ km s}^{-1}$. Exposures taken during ingress and egress are identified with an orange circle in the lower right of each panel. Note that the spectra are not corrected for the velocity offset identified in [subsubsection 5.1.3](#).

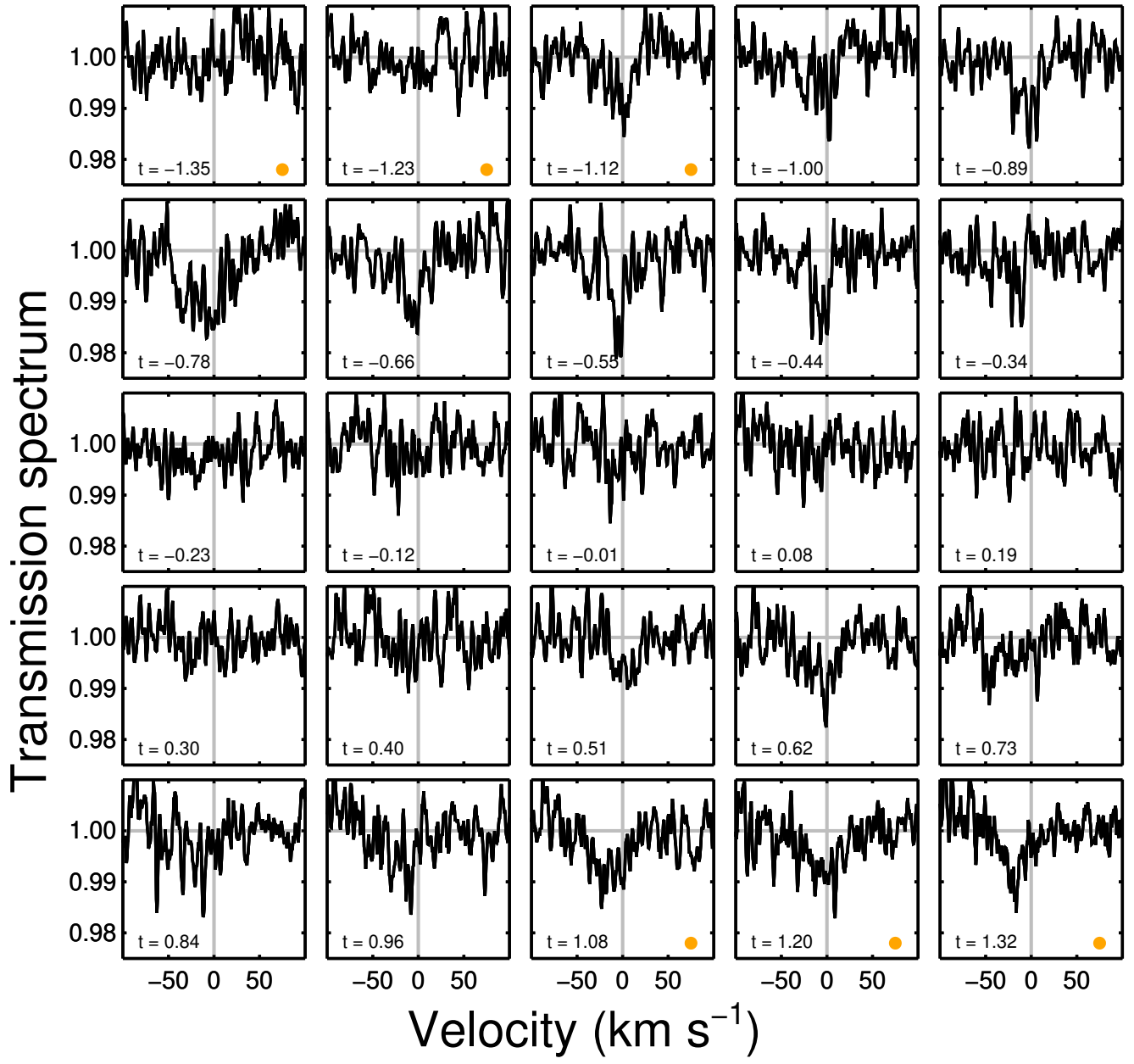


Figure 17. Same as Figure 16 but for H β .